Journal of Computational Physics 236 (2013) 169–186

Contents lists available at SciVerse ScienceDirect

Journal of Computational Physics

journal homepage: www.elsevier.com/locate/jcp

# A robust numerical method for the R13 equations of rarefied gas dynamics: Application to lid driven cavity

Anirudh Rana [a,*], Manuel Torrilhon [b], Henning Struchtrup [a]

[a] Department of Mechanical Engineering University of Victoria, Victoria, BC, Canada
[b] Department of Mathematics, RWTH Aachen University, Aachen, Germany

ARTICLE INFO

*Article history:*
Received 27 April 2012
Received in revised form 22 November 2012
Accepted 23 November 2012
Available online 3 December 2012

*Keywords:*
Kinetic gas theory
R13 equations
Boundary value problem
Lid driven cavity

ABSTRACT

In this work we present a finite difference scheme to compute steady state solutions of the regularized 13 moment (R13) equations of rarefied gas dynamics. The scheme allows fast solutions for 2D and 3D boundary value problems (BVPs) with velocity slip and temperature jump boundary conditions. The scheme is applied to the lid driven cavity problem for Knudsen numbers up to 0.7. The results compare well with those obtained from more costly solvers for rarefied gas dynamics, such as the Integro Moment Method (IMM) and the Direct Simulation Monte Carlo (DSMC) method. The R13 equations yield better results than the classical Navier–Stokes–Fourier equations for this boundary value problem, since they give an approximate description of Knudsen boundary layers at moderate Knudsen numbers. The R13 based numerical solutions are computationally economical and may be considered as a reliable alternative mathematical model for complex industrial problems at moderate Knudsen numbers.



## 1. Introduction

Miniaturization of devices has become an important focus of interest over the past few decades due to the tremendous industrial, commercial and scientific potential. Many miniaturized devices such as hard disk drive heads, inkjet printheads, micro heat-exchangers, micro pumps and turbines involve the flow of gas through microchannels as well as heat exchange and chemical reactions. Processes in such micro-systems are characterized by the Knudsen number (Kn) which is defined as the ratio of the molecular mean-free path of gas particles to a characteristic length scale of the device.

When the Knudsen number is smaller than $\mathrm{Kn} \approx 0.01$, the classical Navier–Stokes–Fourier (NSF) equations with appropriate boundary conditions can be used to describe the process with good accuracy [3,4]. For higher Knudsen numbers, however, the classical equations fail. Indeed, as the Knudsen number grows, so-called rarefaction effects are observed, e.g., velocity slip and temperature jumps at walls, Knudsen boundary layers, heat flux without temperature gradient etc. [3,5]. While jump and slip can be incorporated into the NSF equation by proper boundary conditions, they cannot describe other rarefaction effects.

Microflows are characterized by small length scales or low pressures, and thus have larger Knudsen numbers [1–3]. Flows at all Knudsen numbers are well described by the Boltzmann equation, which must be solved by expensive methods such as Discrete Velocity Schemes [6–11] or the Direct Simulation Monte Carlo Method (DSMC) [12].

The numerical solution of the Boltzmann equation is rather involved, even on modern multi processor computers the solution might take long. In particular in the so-called transition regime, where the Knudsen number is close to unity, solutions might take several days [10,11]. Moreover, the DSMC method implies stochastic noise, in particular for microflows

* Corresponding author.
*E-mail address:* anirudh@uvic.ca (A. Rana).

0021-9991/$ - see front matter © 2012 Elsevier Inc. All rights reserved.
http://dx.doi.org/10.1016/j.jcp.2012.11.023

where the Mach number is very small [13]. Elimination of the noise requires long-time time averages in steady state problems, and averages over large ensembles in transient problems; this makes the method costly [14]. Recently, Hadjiconstaninou and co-workers developed a low-noise Monte-Carlo method which greatly reduces the noise and thus leads to a affordable speed of simulation *for linear problems* [15–17]. The method relies on consideration of the deviation from an equilibrium groundstate, and thus is equivalent to the linearized Boltzmann equation.

Higher-order rarefaction effects can also be predicted by extended macroscopic transport equations, which are derived as approximations to the Boltzmann equation [4]. Classically, extended macroscopic transport equations are derived from the Boltzmann equation either by the Chapman–Enskog (CE) method, which employs an expansion in the Knudsen number [18], or by Grad's moments method, where the distribution function is expressed as a sum of Hermite polynomials [19].

In the CE expansion, the Euler and Navier–Stokes–Fourier equations follow from the zeroth order and first-order expansions, while the second- and third-order expansions lead to the Burnett and super-Burnett equations, respectively [18,20]. The main disadvantages of the classical Burnett and super-Burnett equations is their linear instability in time dependent problems [21,22] and difficulties with the numerical treatment of high order derivatives in the boundary conditions. In contrast, Grad's moment method yields stable equations and simpler boundary conditions, but it is unclear which set of moments one has to take for a given Knudsen number; moreover, the equations yield discontinuous shock structures for high Mach numbers due to their hyperbolic nature [23].

Recently, two of the present authors proposed the regularized 13 moment equations (R13), a macroscopic model based on the asymptotic expansion of the Boltzmann equation [24,39]. The equations are of third order in the Knudsen number, i.e., the same level as super-Burnett equations, and for small enough Knudsen numbers ($\mathrm{Kn} \lesssim 0.5$) the equations describe all known rarefaction effects, like Knudsen layers, Knudsen minimum, heat flux without temperature gradient etc., with good accuracy. The R13 equations were considered first for simple 1D bulk processes, such as stability and sound propagation [24], shock waves [25], and non-linear flow interaction [26]. Then, after the boundary conditions were developed [38,27,28], the R13 equations were used to tackle boundary value problems. Among the problems studied in plane geometry so far are Couette and Poiseuille flow including non-linear analytical solutions [29], transpiration flow [30,31], oscillatory Couette and pulsating Poiseuille flows [31], and acoustic resonators [32]. In [33] the relation between R13 boundary conditions and jump and slip boundary conditions for hydrodynamics was clarified. Geometries with curved boundaries considered so far are cylindrical Couette flow [34], and Poiseuille and transpiration flow in cylindrical pipes [35] as well as in annular channels [36]. Recently, an exact solution for external flow past a sphere was presented [37].

In all of the cited papers, R13 solutions were compared to solutions of the Boltzmann equation or experiments. For all geometries, R13 gives a satisfying agreement to exact data for Knudsen numbers up to $Kn \simeq 0.5$, with some variance between processes. Here one must understand that R13 is an approximation, so that one cannot expect perfect agreement, but must expect some error. For $Kn \leqslant 0.5$, the R13 equations reproduce all flow features, including all rarefaction effects, and give relative errors below 10% [5,31,35]. Moreover, the regularized 13-moment set yields infinite wave speeds, which explain the smooth shock structures over the whole Mach number range [25].

Our main focus for this article lies in the evaluation of the complex equations and mathematical process in a multi-dimensional setting. The numerical method is based on finite differences using a straight forward approach. The lid-driven cavity problem serves as two-dimensional test case. Our results are meant to contribute to the ongoing discussion what moment model gives the best trade-off between accuracy and efficiency. Similar test cases are considered in [40,42,43] with variants of the regularized moment method. A discussion and comparison with these results is given in Section 5.6. Only recently, Xu and co-workers tackled the problem with a unified gas-kinetic scheme, which provides an elegant approach to the Shakov kinetic equation for a discrete velocity model [44,45]. Other computational methods for the R13 equations, such as those proposed in [26,38], are a subject for future research.

Below we will introduce, and use, a numerical simulation method for the two dimensional R13 equations which is computationally economical and provides reliable solutions in good agreement to solutions of the Boltzmann equation. The proposed finite difference scheme allows efficient solutions for 2D boundary value problems (BVPs) of the R13 equations. Special care is taken to incorporate the non-standard boundary condition and total mass constraint. For the original R13 equations, it turns out that the non-linear equations need a higher number of boundary conditions than the linearized equations [28]. As part of the preparation of the equations for the numerical scheme, we use order of magnitude arguments to rewrite the non-linear part of the R13 equations such that the third order accuracy is maintained, but linear and non-linear equations require the same boundary conditions. We shall compare numerical solutions of the driven cavity problem for rarefied gases based on the R13 equations and the NSF equations with slip-jump boundary conditions to kinetic theory solutions. It will be seen that the R13 solutions are in good agreement with kinetic theory solvers for Knudsen numbers up to $\mathrm{Kn} \simeq 0.5$, while NSF results are reliable only up to $\mathrm{Kn} = 0.05$.

## 2. R13 equations

### 2.1. Bulk equations

The regularized 13-moment equations [24] and their corresponding boundary conditions [28] have been derived, described and studied for various cases in [24]-[37]. In this section, we briefly present the nonlinear R13 system for Maxwell molecules. The first five equations are the conservation laws for mass, momentum, and energy,

$$\text{Conservation of mass}: \quad \frac{\partial \rho}{\partial t} + \frac{\partial \rho v_i}{\partial x_i} = 0, \tag{1a}$$

$$\text{Conservation of momentum}: \quad \frac{\partial \rho v_i}{\partial t} + \frac{\partial (p_{ik} + \rho v_i v_k)}{\partial x_k} = \rho G_i, \tag{1b}$$

$$\text{Conservation of total energy}: \quad \frac{\partial \rho e}{\partial t} + \frac{\partial (\rho e v_k + p_{ik} v_i + q_k)}{\partial x_k} = \rho G_i v_i, \tag{1c}$$

where $t$ and $x_i$ are temporal and spatial coordinates, respectively. Moreover, $\rho$, $v_k$, $p_{ik}$, $e$, $G_i$, and $q_k$ denote mass density, velocity, pressure tensor, total energy density, body force, and heat flux, with

$$p_{ij} = p\delta_{ij} + \sigma_{ij} \quad \text{and} \quad e = u + \frac{1}{2}v^2. \tag{2}$$

Here, $u$ denotes the internal density, and $p$ and $\sigma_{ij}$ are the pressure and stress tensor. Also for ideal monatomic gases, $p = \rho\theta = \rho RT$ and $u = \frac{3\theta}{2}$ hold as the equations of state, where $\theta$ is the temperature in energy units, $R$ is the gas constant and $T$ is the thermodynamic temperature.

In the R13 system, heat-flux vector and stress tensor are determined by their balance laws, which read

$$\frac{\partial q_i}{\partial t} + v_k \frac{\partial q_i}{\partial x_k} + \frac{7}{5} q_k \frac{\partial v_i}{\partial x_k} - \sigma_{ik} \frac{\theta}{\rho} \frac{\partial \rho}{\partial x_k} - \frac{\sigma_{ik}}{\rho} \frac{\partial \sigma_{kl}}{\partial x_l} + \frac{5}{2} \sigma_{ik} \frac{\partial \theta}{\partial x_k} + \theta \frac{\partial \sigma_{ik}}{\partial x_k} + \frac{7}{5} q_i \frac{\partial v_k}{\partial x_k} + \frac{2}{5} q_k \frac{\partial v_k}{\partial x_i} + \frac{1}{2} \frac{\partial R_{ik}}{\partial x_k} + \frac{1}{6} \frac{\partial \Delta}{\partial x_i} + m_{ikl} \frac{\partial v_k}{\partial x_l} + \frac{5}{2} p \frac{\partial \theta}{\partial x_i} = -\frac{2}{3} \frac{p}{\mu} q_i, \tag{3}$$

$$\frac{\partial \sigma_{ij}}{\partial t} + v_k \frac{\partial \sigma_{ij}}{\partial x_k} + \frac{\partial m_{ijk}}{\partial x_k} + \frac{4}{5} \frac{\partial q_{\langle i}}{\partial x_{j\rangle}} + 2\sigma_{k\langle i} \frac{\partial v_{j\rangle}}{\partial x_k} + \sigma_{ij} \frac{\partial v_k}{\partial x_k} + 2p \frac{\partial v_{\langle i}}{\partial x_{j\rangle}} = -\frac{p}{\mu} \sigma_{ij}, \tag{4}$$

For $\Delta = R_{ij} = m_{ijk} = 0$ the above equations reduce to the well-known 13 moment equations of Grad [19]. The R13 equations result from taking into account the appropriate terms of higher order moment equations as, see [24,4] for details,

$$\Delta = -\frac{\sigma_{kl}\sigma_{kl}}{\rho} + 6\frac{\sigma_{kl}\sigma^{NSF}_{kl}}{\rho} + \frac{56}{5}\frac{q_k q^{NSF}_k}{p} - 12\frac{\mu}{p}\left(\theta\frac{\partial q_k}{\partial x_k} - \theta q_k \frac{\partial \ln p}{\partial x_k}\right), \tag{5}$$

$$R_{ij} = -\frac{4}{7}\frac{\sigma_{k\langle i}\sigma_{j\rangle k}}{\rho} + \frac{24}{7}\frac{\sigma_{k\langle i}\sigma^{NSF}_{j\rangle k}}{\rho} + \frac{192}{75}\frac{q_{\langle i}q^{NSF}_{j\rangle}}{p} - \frac{24}{5}\frac{\mu}{p}\left(\theta\frac{\partial q_{\langle i}}{\partial x_{j\rangle}} - \theta q_{\langle i}\frac{\partial \ln p}{\partial x_{j\rangle}}\right),$$

$$m_{ijk} = \frac{8}{15}\frac{\sigma_{\langle ij}q^{NSF}_{k\rangle}}{p} + \frac{4}{5}\frac{q_{\langle i}\sigma^{NSF}_{jk\rangle}}{p} - 2\frac{\mu}{p}\left(\theta\frac{\partial \sigma_{\langle ij}}{\partial x_{k\rangle}} - \theta\sigma_{\langle ij}\frac{\partial \ln p}{\partial x_{k\rangle}}\right).$$

The indices inside angular brackets denote the symmetric trace-free part of tensors [4]. For instance, when$A_{\langle ij\rangle}$ and $A_{\langle ijk\rangle}$ are the symmetric parts of the tensors $A_{ij}$ and $A_{ijk}$, then

$$A_{\langle ij\rangle} = A_{(ij)} - \frac{1}{3}A_{kk}\delta_{ij},$$
$$A_{\langle ijk\rangle} = A_{(ijk)} - \frac{1}{5}\left(A_{(llk)}\delta_{ij} + A_{(llj)}\delta_{ik} + A_{(lli)}\delta_{jk}\right).$$

In (5) we introduced the abbreviations $\sigma^{NSF}_{ij}, q^{NSF}_i$ for the Navier–Stokes and Fourier laws, i.e.,

$$\sigma^{NSF}_{ij} = -2\mu\frac{\partial v_{\langle i}}{\partial x_{j\rangle}} \quad \text{and} \quad q^{NSF}_i = -\kappa\frac{\partial \theta}{\partial x_i}, \tag{6}$$

where $\mu$ and $\kappa = \frac{15}{4}\mu$ are the coefficients of viscosity and thermal conductivity, respectively.

### 2.2. Boundary conditions

Maxwell's accommodation model [3,4] for the boundary conditions in kinetic theory was used to derive boundary conditions for the R13 system, which link the moments of the gas in front of the wall to the tangential wall velocity $v^W_\tau$ and wall temperature $\theta^W$. The details of the construction procedure for the boundary conditions (BCs) for the R13 equations can be found in [28], the final result reads

$$v_n = 0 \tag{7a}$$

$$\sigma_{\tau n} = \frac{-\chi}{2-\chi}\sqrt{\frac{2}{\pi\theta}}\left(\mathcal{P}\mathcal{V}_\tau + \frac{1}{5}q_\tau + \frac{1}{2}m_{\tau nn}\right), \tag{7b}$$

$$q_n = \frac{-\chi}{2-\chi}\sqrt{\frac{2}{\pi\theta}}\left(2\mathcal{P}\mathcal{T} - \frac{1}{2}\mathcal{P}\mathcal{V}_\tau^2 + \frac{1}{2}\theta\sigma_{nn} + \frac{1}{15}\Delta + \frac{5}{28}R_{nn}\right), \tag{7c}$$

$$R_{\tau n} = \frac{\chi}{2-\chi}\sqrt{\frac{2}{\pi\theta}}\left(6\mathcal{P}\mathcal{T}\mathcal{V}_\tau + \mathcal{P}\theta\mathcal{V}_\tau - \mathcal{P}\mathcal{V}_\tau^3 - \frac{11}{5}\theta q_\tau - \frac{1}{2}\theta m_{\tau nn}\right), \tag{7d}$$

$$m_{nnn} = \frac{\chi}{2-\chi}\sqrt{\frac{2}{\pi\theta}}\left(\frac{2}{5}\mathcal{P}\mathcal{T} - \frac{3}{5}\mathcal{P}\mathcal{V}_\tau^2 - \frac{7}{5}\theta\sigma_{nn} + \frac{1}{75}\Delta - \frac{1}{14}R_{nn}\right), \tag{7e}$$

$$m_{\tau\tau n} = \frac{-\chi}{2-\chi}\sqrt{\frac{2}{\pi\theta}}\left(\frac{1}{5}\mathcal{P}\mathcal{T} - \frac{4}{5}\mathcal{P}\mathcal{V}_\tau^2 + \frac{1}{14}R_{\tau\tau} + \theta\sigma_{\tau\tau} - \frac{1}{5}\theta\sigma_{nn} + \frac{1}{150}\Delta\right) \tag{7f}$$

where

$$\mathcal{P} = \rho_W\sqrt{\theta_W}\sqrt{\theta} = \left(\rho\theta + \frac{1}{2}\sigma_{\tau\tau} - \frac{1}{120}\frac{\Delta}{\theta} - \frac{1}{28}\frac{R_{\tau\tau}}{\theta}\right),$$

and $V_\tau = v_\tau - v_\tau^W$ and $T = \theta - \theta_W$ are slip velocity and temperature jump, respectively. Obviously, all quantities appearing in the boundary conditions must be evaluated at the wall. Thus, $\{\rho, v_i, \theta, \sigma_{ij}, q_i\}$ are the variables at the wall, and $\{\Delta, R_{ij}, m_{ijk}\}$ are the higher moments as given by (5) evaluated at the wall. Moreover, $\tau$ and $n$ denote the tangential and normal components of the tensors, where the wall normal is pointing toward the gas. The only parameter occurring in the boundary conditions is the Maxwell accommodation coefficient $\chi$. The accommodation coefficient assumes values $0 \leqslant \chi \leqslant 1$, where $\chi = 1$ for full accommodation, i.e., thermalization of gas particles with the wall, and $\chi = 0$ for no accommodation, i.e., specular reflection of gas particles at the wall.

The macroscopic boundary conditions (7a)–(7f) result from taking moments of a Grad distribution function for 26 moments to describe the gas particles travelling towards the wall, and then computing the particles leaving the wall from this distribution and the Maxwell interaction kernel, see [28,5] for details. Accordingly, the boundary conditions themselves are local, since they depend only on the 26 moments $\{\rho, v_i, T, \sigma_{ij}, q_i, \Delta, R_{ij}, m_{ijk}\}$ that describe the gas right at the wall, and on the local temperature $\theta_W$ and velocity $v_\tau^W$ of the wall. Nonlocality, and thus effects of curvature, enters the boundary conditions from replacing the higher moments $\{\Delta, R_{ij}, m_{ijk}\}$by their constitutive equations (5) which include gradients and divergences. For curved surfaces, additional curvature effects, due to the mutual influence between boundary conditions and the bulk PDE's needs further investigation which will be considered somewhere else in the future. In [35–37], we have studied cylindrical flows and flow past a sphere, and the proceedings outlined in these papers show how curvature effects influence the boundary conditions.

The boundary conditions (7a)–(7c) can also be used to derive first order slip and jump boundary conditions for the Navier–Stokes–Fourier equations by replacing, $\sigma_{ij} = \sigma_{ij}^{NSF}$ and $q_i = q_i^{NSF}$ from Eq. (6), in Eqs. (7a)–(7c) as [33]

$$v_n = 0 \tag{8}$$

$$\sigma_{\tau n} = \frac{-\chi}{2-\chi}\sqrt{\frac{2}{\pi\theta}}\left(\mathcal{P}\mathcal{V}_\tau - \frac{1}{5}\kappa\frac{\partial T}{\partial x_\tau}\right), \tag{9}$$

$$q_n = \frac{-\chi}{2-\chi}\sqrt{\frac{2}{\pi\theta}}\left(2\mathcal{P}\mathcal{T} - \frac{1}{2}\mathcal{P}\mathcal{V}_\tau^2 - \mu\theta\frac{\partial v_{\langle n}}{\partial x_{n\rangle}}\right), \tag{10}$$

Second order boundary conditions for NSF can also be obtained by combining the R13 boundary conditions and replacing the stress tensor and heat flux vector using the Burnett equations [33,35], these are presented in Appendix B.

## 3. Model problem: lid driven cavity

The lid driven cavity is a classical benchmark problem in fluid mechanics, that, in spite of its simple geometry, exhibits most of the features of more complicated process described by the kinetic equation. Here, we consider a monatomic rarefied gas contained in a square enclosure with length $L$, see Fig. 1. The boundaries at $x = 0, x = L$, and $y = 0$ are stationary, while the upper boundary at $y = L$ is in motion with a constant horizontal velocity $v_{lid}$. All the walls are considered isothermal with a temperature $T_0 = 273$ K and the lid-velocity was chosen such that $v_{lid}/\sqrt{RT_0} \ll 1$. The domain is considered as unbounded in the $z$-direction and the effects in that direction are neglected.

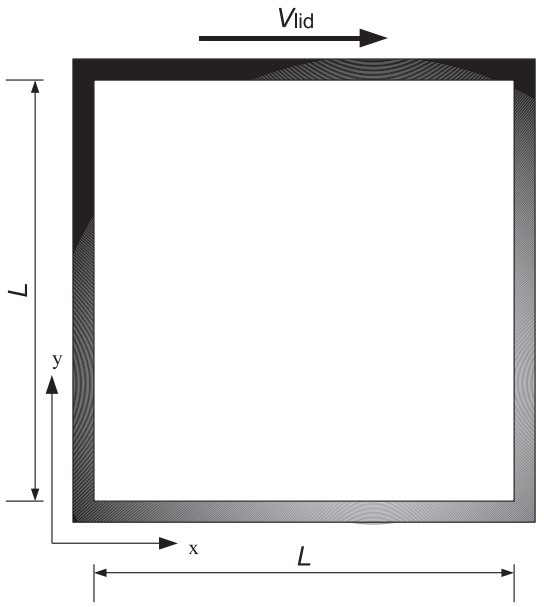


**Fig. 1.** Schematic of lid driven cavity.

For convenience, some results will be presented in a dimensionless form defined as

$$\widehat{x}_i = \frac{x_i}{L}, \quad \widehat{\theta} = \frac{\theta}{\theta_0}, \quad \widehat{\rho} = \frac{\rho}{\rho_0}, \quad \widehat{v}_i = \frac{v_i}{\sqrt{\theta_0}},$$
$$\widehat{q}_i = \frac{q_i}{\rho_0 \sqrt{\theta_0}^3}, \quad \text{and} \quad \widehat{\sigma}_{ij} = \frac{\sigma_{ij}}{\rho_0 \theta_0},$$

where $x$ and $y$ are the horizontal and vertical axis, respectively, and $\rho_0$ is the initial density. The corresponding Knudsen number is given by

$$\mathrm{Kn} = \frac{\mu_0}{\rho_0 \sqrt{\theta_0}} \frac{1}{L},$$

where $\mu_0$ is the viscosity of the gas based on the reference temperature $T_0$.

Sharipov and co-workers solved kinetic equations for this problem for various values of the rarefaction parameter $\delta = \sqrt{\frac{1}{2}\frac{1}{\mathrm{Kn}}}$ [6]. These results will serve us for comparison. DSMC solutions to the problem are presented in [42].

## 4. Numerical method

We shall present our scheme for 2D steady state problems in rectangular domains. The restriction to cartesian grids is done for simplicity as a first approach. However, there is no fundamental difficulty that prevents the method to be applied to more general geometries. For example, curvilinear structured grids could be included by using the local mesh mapping function and interpolation to discretize the derivatives. The structure of the resulting (non-) linear system would remain the same. An extension to three dimensions is also possible. However, 3D and more general geometries are left for future work.

For preparation we write the dimensionless partial differential equations (1)–(5) as a first order system,

$$\mathcal{A}(U)\frac{\partial U}{\partial x} + \mathcal{B}(U)\frac{\partial U}{\partial y} + \frac{1}{Kn}P(U)U = 0. \tag{11}$$

Here,

$$U = \left[\rho \quad v_x \quad v_y \quad \theta \quad q_x \quad q_y \quad \sigma_{xx} \quad \sigma_{xy} \quad \sigma_{yy} \quad R_{xx} \quad R_{xy} \quad R_{yy} \quad m_{xxx} \quad m_{xyy} \quad m_{xxy} \quad m_{yyy} \quad \Delta\right],$$

is the vector of field variables, and $\mathcal{A}(U)$ and $\mathcal{B}(U)$ are the coefficient matrices in $x$- and $y$-directions, respectively. The matrix $P(U)$is the production matrix. Since we only consider steady state flow, $\frac{\partial}{\partial t} \equiv 0$ in Eqs. (1a)–(1c), (2)–(4). The matrices $\mathcal{A}(U), \mathcal{B}(U)$ and $P(U)$are presented in Appendix A.

### 4.1. Coherence of boundary conditions

For a boundary-value problem, a suitable set of boundary conditions must be prescribed to avoid the nonexistence or non-uniqueness of the solution. For any first order system of equations, the required number of boundary conditions is equal to the number of integration constants obtained through integration with respect to the space variables, $x$ and $y$.

For convenience let us consider the $x$-direction only, however, a similar argument will hold for an arbitrary direction. If $\mathcal{N}$ is the dimension of the system (11) and the matrix $\mathcal{A}(U)$has a zero eigenvalue with multiplicity $\alpha$, then we must describe $\mathcal{N}-\alpha$ boundary conditions [28]. Moreover, the normal convective flux vanishes, i.e., $v_x = 0$, at a point infinitesimally close to a non-permeable wall, therefore one has to take into account the eigenvalues of the matrix $\mathcal{A}(U : v_x = 0)$.

A detailed inspection of the coefficient matrices $\mathcal{A}(U)$ and $\mathcal{B}(U)$shows that $\mathcal{A}(U : v_x = 0)$ and $\mathcal{B}(U : v_y = 0)$possess a zero eigenvalue with multiplicity $\alpha = 3$, thus one needs to prescribe $17-3 = 14$ conditions altogether for the $x$- and $y$-directions, respectively.

On the other hand, if a small deviation from equilibrium is considered and the matrix $\mathcal{A}(U)$is linearized with respect to the equilibrium state $U_0$, where

$$U_0 = \left[\rho_0, \quad 0, \quad 0, \quad \theta_0, \quad \mathbf{0} \in \mathbb{R}^{13}\right],$$

then the linearized matrix $\mathcal{A}(U_0)$has a zero eigenvalue with multiplicity 5, thus the integrations requires $17-5 = 12$ boundary conditions for each direction. These 12 boundary conditions are precisely Eqs. (7a)–(7f) at $x = 0$ and $x = L$, respectively.

Thus, it seems that a different number of boundary conditions is required for the linearized and the fully non-linear equations. The hypothesis of coherence of boundary conditions [28] states that, *"The transition from a process in the linear regime to a non-linear process should not change the number of boundary conditions"*. That is, describing a non-linear process with R13 should not require more boundary conditions than in the linear case. To avoid this inconsistency, we reformulate the constitutive relations in Eqs. (5), without altering the third order asymptotic accuracy of the equations. For this, the Navier–Stokes stress and the Fourier heat flux in the R13 constitutive Eqs. (5) are replaced by the actual stress and heat flux as, see (6),

$$\begin{aligned} \sigma_{ij}^{NSF} &= -2\mu\frac{\partial v_{\langle i}}{\partial x_{j\rangle}} = \sigma_{ij} + \mathcal{O}(\mathrm{Kn}^2) \quad \text{and} \\ q_i^{NSF} &= -\kappa\frac{\partial T}{\partial x_i} = q_i + \mathcal{O}(\mathrm{Kn}^2), \end{aligned} \tag{12}$$

to obtain instead of (5)

$$\begin{aligned} \Delta &= 5\frac{\sigma_{kl}\sigma_{kl}}{\rho} + \frac{56}{5}\frac{q_k q_k}{p} - 12\frac{\mu}{p}\left(\theta\frac{\partial q_k}{\partial x_k} - \theta q_k\frac{\partial \ln p}{\partial x_k}\right), \\ R_{ij} &= \frac{20}{7}\frac{\sigma_{k\langle i}\sigma_{j\rangle k}}{\rho} + \frac{192}{75}\frac{q_{\langle i}q_{j\rangle}}{p} - \frac{24}{5}\frac{\mu}{p}\left(\theta\frac{\partial q_{\langle i}}{\partial x_{j\rangle}} - \theta q_{\langle i}\frac{\partial \ln p}{\partial x_{j\rangle}}\right), \\ m_{ijk} &= \frac{20}{15}\frac{q_{\langle i}\sigma_{jk\rangle}}{p} - 2\frac{\mu}{p}\left(\theta\frac{\partial \sigma_{\langle ij}}{\partial x_{k\rangle}} - \theta\sigma_{\langle ij}\frac{\partial \ln p}{\partial x_{k\rangle}}\right). \end{aligned} \tag{13}$$

This transformation introduces an asymptotic error of $\mathcal{O}(\mathrm{Kn}^3)$ in the expressions for $\Delta, R_{ij}, m_{ijk}$: the changed terms appear as a multiples of stress, $\sigma_{ij}$ and heat flux, $q_i$, which both are of first order in Knudsen number, $\mathcal{O}(\mathrm{Kn})$. Therefore the error $\mathcal{O}(\mathrm{Kn}^2)$ in (12) is multiplied by a first order quantity, which results in a third order error in the constitutive equations. The overall asymptotic accuracy of the R13 system remains at third order, $\mathcal{O}(\mathrm{Kn}^3)$.

Replacing the original constitutive equations (5) by the new equations (13) results in new matrices $\mathcal{A}(U)$ and $\mathcal{B}(U)$, which, as is easy to show, possess a zero eigenvalue with multiplicity $\alpha = 5$, thus one needs only the 12 boundary conditions (7a)–(7f), which is the same as the linearized case. The new matrices $\mathcal{A}(U)$ and $\mathcal{B}(U)$ are presented in Appendix A.

A similar transformation was suggested in [28] where pressure gradients in (5) were replaced by means of the steady state momentum balance. The transformation shown above has the following advantages: (1) No pressure gradients are replaced; consequently, this transformation is justified even in presence of high pressure gradients or strong body forces. (2) The transformation rule is obtained for the full 3D R13 equations rather then for a simplified geometry as in [28]; therefore the transformation can be performed for arbitrary geometry and dimensions.

The new transformation, which will be used from now on, gives consistency of boundary conditions such that the linear and the non-linear R13 equations require the same boundary conditions. For higher order models such as R20, R26 [40,41] this approach can be generalized.

### 4.2. Finite difference approximation

We discretize the spatial domain using $N\times M$ grid points as $x_i = i\Delta x$ and $x_j = j\Delta y$, where $i = 0, N+1$ and $j = 0, M+1$ are the boundary nodes. Using this discretization, Eq. (11) assumes the form

$$\mathcal{A}_{i,j}\frac{\partial U_{i,j}}{\partial x} + \mathcal{B}_{i,j}\frac{\partial U_{i,j}}{\partial y} + \frac{1}{Kn}P_{i,j}U_{i,j} = 0 \forall (i,j) \in [1,N]\times[1,M], \tag{14}$$

where $U_{i,j} = U(x_i, y_j), \mathcal{A}_{i,j} = \mathcal{A}(U_{i,j})$ etc.

The boundary conditions (7a)–(7f) are incorporated in matrix form, and linear extrapolation is used for boundary nodes to obtain

$$U_{0,j} = \mathcal{X}^{+}_{1,j}(2U_{1,j} - U_{2,j}) + \mathcal{X}^{d+}_{1,j}\,, \tag{15a}$$

$$U_{N+1,j} = \mathcal{X}^{-}_{N,j}(2U_{N,j} - U_{N-1,j}) + \mathcal{X}^{d-}_{N,j} \;\forall j \in [1,M], \tag{15b}$$

$$U_{i,0} = \mathcal{Y}^{+}_{i,1}(2U_{i,1} - U_{i,2}) + \mathcal{Y}^{d+}_{i,1}\,, \tag{16a}$$

$$U_{i,M+1} = \mathcal{Y}^{-}_{i,j_{m+1}}(2U_{i,M} - U_{i,M-1}) + \mathcal{Y}^{d-}_{i,M} \;\forall i \in [1,N], \tag{16b}$$

for $x$ – walls (wall normal pointing in the $x$ direction) and $y$ – walls (wall normal pointing in the $y$ direction), respectively. Here, the matrix $\mathcal{X}_{1j}$(or $\mathcal{Y}_{1j}$), is the corresponding coefficient matrix of field variables $U$ in Eqs. (7a)–(7f) for $x$ – walls (or $y$ – walls), and the vector $\mathcal{X}^{d}_{1j}$(or $\mathcal{Y}^{d}_{1j}$) consists of inhomogenities due to wall properties $(\theta^W, v^W)$on $x$ – walls (or $y$ – walls), refer to the appendix A for the explicit expressions for $\mathcal{X}^{\pm}_{1,j}$. The superscripts " +" and "-", denote the positive and negative directions of the wall normal, i.e., $n_x = \pm 1$ (or $n_y = \pm 1$), respectively. In the boundary matrices, $\mathcal{X}^{\pm}_{1,j}$, only the rows for the variables $\{\, v_x \quad q_x \quad \sigma_{xy} \quad R_{xy} \quad m_{xxx} \quad m_{xyy} \,\}$ give boundary conditions, while the other rows give identities.

By replacing the derivatives in Eq. (14) using a central difference scheme we get

$$\mathcal{A}_{ij}\frac{U_{i+1,j}}{2\Delta x} - \mathcal{A}_{ij}\frac{U_{i-1,j}}{2\Delta x} + \mathcal{B}_{ij}\frac{U_{i,j+1}}{2\Delta y} - \mathcal{B}_{ij}\frac{U_{i,j-1}}{2\Delta y} + \frac{1}{Kn}P_{ij}U_{i,j} = 0 \forall (i,j) \in [2,N-1]\times[2,M-1]. \tag{17}$$

Combining Eq. (17) with Eq. (15a), we obtain the equation for the left wall ($i = 1$)

$$\left(\frac{1}{Kn}P_{1,j} - \frac{1}{\Delta x}\mathcal{A}_{1,j}\mathcal{X}^{+}_{1,j}\right)U_{1,j} + \frac{1}{2\Delta x}\mathcal{A}_{1,j}\left(I + \mathcal{X}^{+}_{1j}\right)U_{2,j} + \mathcal{B}_{1,j}\frac{U_{1,j+1}}{2\Delta y} - \mathcal{B}_{1,j}\frac{U_{1,j-1}}{2\Delta y} = \frac{1}{2\Delta x}\mathcal{A}_{1,j}\mathcal{X}^{+d}_{1j} \;\forall j \in [2,M-1]. \tag{18}$$

Correspondingly, for the right wall ($i = N$) we combine the Eq. (17) with Eq. (15b), to get

$$\left(\frac{1}{Kn}P_{N,j} + \frac{1}{\Delta x}\mathcal{A}_{N,j}\mathcal{X}^{-}_{N,j}\right)U_{N,j} - \frac{1}{2\Delta x}\mathcal{A}_{N,j}\left(I + \mathcal{X}^{-}_{N,j}\right)U_{N-1,j} + \mathcal{B}_{N,j}\frac{U_{N,j+1}}{2\Delta y} - \mathcal{B}_{N,j}\frac{U_{N,j-1}}{2\Delta y} = -\frac{1}{2\Delta x}\mathcal{A}_{N,j}\mathcal{X}^{-d}_{N,j} \;\forall j \in [2,M-1]. \tag{19}$$

A similar treatment is used for the lower ($j = 0$) and the upper wall ($j = M$). In the same manner, corners are dealt with, for example for the lower-left corner ($i = 1, j = 1$) we have

$$\begin{aligned}&\left(\frac{1}{Kn}P_{11} - \frac{1}{\Delta x}\mathcal{A}_{11}\mathcal{X}^{+}_{11} - \frac{1}{\Delta y}\mathcal{B}_{11}\mathcal{Y}^{+}_{11}\right)U_{1,1} + \frac{1}{2\Delta x}\mathcal{A}_{11}(I + \mathcal{X}^{+}_{11})U_{2,1} + \frac{1}{2\Delta y}\mathcal{B}_{11}(I + \mathcal{Y}^{+}_{11})U_{1,2}\\ &\quad = \frac{1}{2\Delta x}\mathcal{A}_{11}\mathcal{X}^{+d}_{11} + \frac{1}{2\Delta y}\mathcal{B}_{11}\mathcal{Y}^{+d}_{11}.\end{aligned} \tag{20}$$

Combining all discrete values into the vector $X = \{U_{i,j}\}_{(i,j)\in[1,N]\times[1,M]}$ we can write the above equations in compact matrix form,

$$\mathcal{M}(X)X = \mathfrak{b}(X). \tag{21}$$

### 4.3. Non-local boundary condition

During the process the total mass inside the cavity is conserved, which gives one additional non-local-boundary condition,

$$\int_{x=0}^{L}\int_{y=0}^{L}\varrho(x,y)dxdy = M_0. \tag{22}$$

Problems involving non-local boundary conditions have been studied in many papers, such as [46,47]. Here, we present an alternative approach.

Eq. (21) is nonlinear in the discretized variable vector $X$ and therefore an iterative scheme must be used to solve it. To ensure the total mass constraint (22) at each iteration, the following strategy is proposed:

A detailed inspection of the matrix $\mathcal{M}(X)$shows that it has a unique $(\forall X)$ right null space of one dimension, spanned by $X^R$, i.e., $\mathcal{M}(X)X^R = 0$. Existence of a null space implies that if $X^p$ is some particular solution of Eq. (21), so is $X^p + \alpha X^R \;\forall \alpha \in \mathbb{R}$.

Computation (using Mathematica) of the null vector $X^R$ shows that it has non-zero elements only for the local densities $\rho_{i,j}$. Therefore, the density $\rho$ can only be computed up to a constant $\alpha$, which needs to be determined using the total mass constraint, given by Eq. (22).

The total mass constraint can be written in discrete form using the trapezoidal rule as

$$\sum_{r=1}^{N.M} w_r X_r = M_0, \tag{23}$$

where $w_r$ are the corresponding weight functions. Eq. (23) allows to recast the system (21) as

$$\widetilde{\mathcal{M}}(X)\widetilde{X} = \tilde{\mathfrak{b}}(X) \tag{24}$$

where

$$\widetilde{\mathcal{M}}(X) = \begin{bmatrix} 0 & \mathbf{w}^T \\ X^L & \mathcal{M}(X) \end{bmatrix}, \quad \widetilde{X} = \begin{bmatrix} \alpha \\ X \end{bmatrix}, \quad \tilde{\mathfrak{b}}(X) = \begin{bmatrix} M_0 \\ \mathfrak{b}(X) \end{bmatrix}. \tag{25}$$

and $X^L$is the left null space of the matrix $\mathcal{M}(X)$.

It is obvious from the first row of the system (24) that any solution of (24) also satisfies the total mass constraint given by Eq. (23).

The following discussion will lead to the understanding of the second row. Let us assume that the system (21) has at least one solution. Then for all solutions $X$

$$X^L\mathfrak{b}(X) = 0, \tag{26}$$

and any solution of (24) will also be a solution of (21) as will be shown now.

The second block of the system (24) reads

$$\alpha X^L + \mathcal{M}(X)X = \mathfrak{b}(X); \tag{27}$$

multiplication with the left null vector $X^L$ gives

$$\alpha X^L \cdot X^L + X^L \cdot \mathcal{M}(X)X = X^L\mathfrak{b}(X). \tag{28}$$

Since $X^L$ is a null vector of $\mathcal{M}$ this reduces to

$$\alpha X^L \cdot X^L = X^L\mathfrak{b}(X);$$

and with the solvability condition (26) and $X^L \cdot X^L \neq 0$, we find $\alpha = 0$, and thus (27) reduces to (21).

The non-linear system Eq. (24) is solved for $\widetilde{X} = (\alpha, X)$by fixed point iterative scheme, where in each iteration the linear system of equations is solved using an iterative solver. The quasi minimal residual (QMR) iterative scheme was chosen for this paper due to the robustness of the method [48]. As a starting value for the iteration, a global equilibrium state is used. Therefore, the linear R13 (or NSF) equations are solved in the first iteration.

### 4.4. Algorithm

The solution of the system (24) is done iteratively in the following steps:

- Step 1:
  The values of the variables at all grid points are initialized as a global equilibrium state at rest, with global density $\rho_0 = p_0/\theta_0$ and global temperature $\theta_0$; initially the values of all other fields are zero, thus
  $$X_{i,j}^{(0)} = U_{i,j}^{(0)} = \begin{bmatrix} \rho_0 & 0 & 0 & \theta_0 & \mathbf{0} \in \mathbb{R}^{13} \end{bmatrix}.$$
- Step 2:
  Eq. (24) is solved with the iterative solver QMR [48], which solves $\widetilde{\mathcal{M}}\left(X^{(k)}\right)\widetilde{X}^{(k+1)} = \tilde{\mathfrak{b}}(X^{(k)})$ for $\widetilde{X}^{(k+1)}$.
- Step 3:
  If $\left\|X^{k+1} - X^k\right\|_1 \leqslant \epsilon$ holds, the computation is stopped, else Step 2 is done again. We used $\varepsilon = 10^{-6}$ [$\sim \mathcal{O}(\Delta x^3, \Delta x^3)$].
  The discretization in the computational domain has been progressively refined to ensure the grid independence of the results.

### 4.5. Empirical order of convergence

The numerical error of the approximate solution can be estimated using the empirical order of convergence. An $L_1$-norm is used to calculate the error, defined as

$$||(\varrho^{Exact} - \varrho^{Num})||_1 = \Delta x \Delta y \sum_{i=1}^{N}\sum_{j=1}^{M} |\varrho_{ij}^{Exact} - \varrho_{ij}^{Num}|, \tag{29}$$

where the exact solution is approximated on a very refined mesh with 500×500 cells. Fig. 2(a) shows the $\log_{10}$-$\log_{10}$ plots of the error estimates for dimensionless velocity with respect to the mesh size $N$, for Knudsen numbers $\mathrm{Kn} = 0.5$ (greencurves), $0.1$(bluecurves) and $0.05$ (redcurves). These results were computed for the driven cavity with $V_{lid} = 50m/s$ on the a computational domain $[0,1] \times [0,1]$. Fig. 2(a) shows an approximately second order convergence at all Knudsen numbers.

For determining an appropriate mesh configuration a grid independence test is conducted as well, where different meshes of size $N_i = 40, 50, 75, 100, 200, 400$ are tested. Relative percentage changes in dimensionless velocity ($\hat{v}_x = v_x/v_{lid}$) along the moving wall was monitored as the grid was refined successively. The results are plotted in

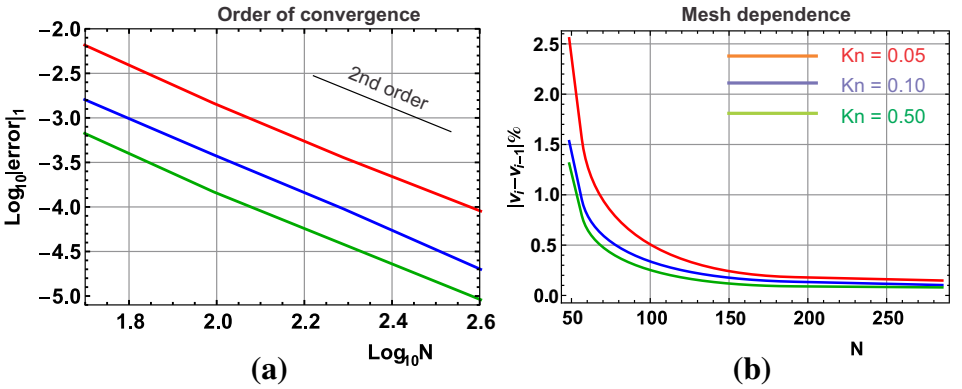


**Fig. 2.** (a) Empirical order convergence for velocity $v_x$, and (b) mesh dependence of the numerical solution for $v_x$ along the lid, for Knudsen numbers Kn = 0.5(greencurves), 0.1(bluecurves)and0.05(redcurves).

Fig. 2(b), for Knudsen numbers Kn = 0.5, 0.1 and 0.05. It is evident from Fig. 2(b) that the relative percentage change in dimensionless velocity between two successive grid sizes is less then 1% as the grid is refined beyond 75 × 75.

With our un-optimized Matlab code used on a standard PC with a 75 × 75 grid, the solution of the non-linear R13 equations requires about 15 min, while the solution based upon the DSMC method takes days for a similar problem.

## 5. Results and discussion

In this section, numerical solutions for the 2D driven cavity are presented for the R13 equations and the Navier–Stokes–Fourier equations with first and second order boundary conditions, and compared with exact kinetic theory computations based on DSMC [42,40] and IMM [6].

### 5.1. One-dimensional profiles

The left and right parts of Fig. 3 show the profiles of the dimensionless vertical component of the velocity, $\frac{v_y}{v_{lid}}$, along the vertical centerline of the cavity, and the dimensionless horizontal component of the velocity, $\frac{v_x}{v_{lid}}$, along the horizontal line crossing the centre of the vortex, respectively, at different values of the Knudsen number Kn. For small Knudsen numbers (1st and 2nd rows of Fig. 3) all models (NSF with 1st and 2nd order BCs, R13) exhibit a good agreement with DSMC.

For the larger Knudsen number $Kn = 0.4$, the results are shown in the third row of Fig. 3. The NSF equations with first and second order boundary conditions have lost their validity completely, as they fail not only to describe the slip and the Knudsen layer at the wall, but also cannot match the velocity in the bulk. The R13 equations, on the other hand, reproduce the velocity profiles in the bulk with rather good accuracy. Near the wall, where Knudsen layers dominate the flow, we observe some discrepancy which is due to the R13 equations' insufficient solution of the Knudsen layer [33], see below.

In Fig. 4 we comparethe temperature profile along a vertical plane crossing the center of the cavity, for Kn = 0.08 and 0.4.Due to the relatively low lid velocity frictional heating is rather weak, so that the temperature deviates only slightly from the wall temperature of 273 K. In this case NSF with 1st order boundary conditions does well for the smaller Knudsen number, but for the larger value it underpredicts the temperature near the moving wall. NSF with 2nd order boundary conditions substantially overpredicts the temperature in both cases.

The R13 equations, on the other hand, predict the thermal behavior of the flow with reasonable accuracy for both Knudsen numbers.

### 5.2. Knudsen layers

A detailed examination of a simple kinetic equation [49] has shown that in extended moment equations the Knudsen layer appears as a superposition of several exponential layers with different spatial decay; the decay coefficients are eigenvalues of a coefficient matrix that follows from the bulk equations. Moment methods with few moments have only few layers for the superposition, and thus cannot match the details of the Knudsen layers. The results indicate that boundary jumps compensate for the lack of accuracy of the Knudsen layers such that the bulk flow is described well. This, indeed is what we observe in Fig. 3, where the R13 wall slip and Knudsen layer both differ from the exact solution, but the bulk result is met closely.

In [41] Gu and Emerson have computed Poiseuille flow with the R13 and R26 equations, where the latter, since they have more moments, have additional contributions to the Knudsen layers. These additional layers lead to improvement over the R13 equations for Knudsen layer dominated problems, in particular when the Knudsen number becomes so large that the Knudsen layer extends over the complete flow domain, from wall to wall. In extension to the observation in [49,41] it is expected that higher moment methods such as R20 [40] or R26 will be able to describe the flow properties more accurately. We

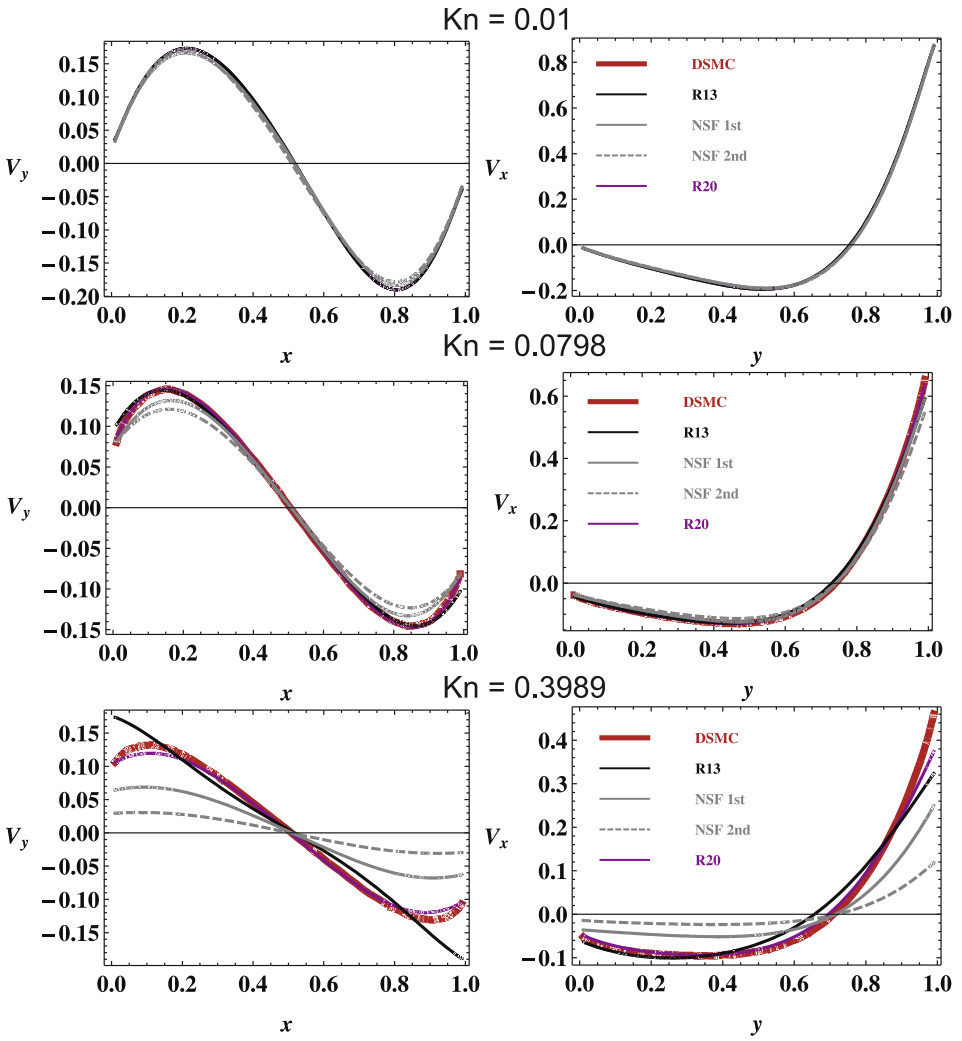


**Fig. 3.** Profiles of the $y$-component of the velocity, $v_y/v_{lid}$, *(left) on a horizontal plane crossing the center of the main vortex and the profiles of the* $x$*-component of the velocity* $v_x/v_{lid}$*, (right) on a vertical plane crossing the center of the cavity, for various values of* Kn and for $v_{lid} = 50m/s$.

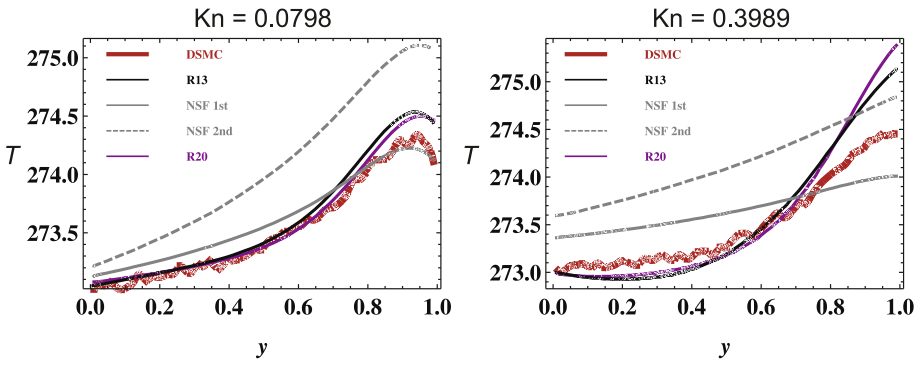


**Fig. 4.** Comparison of the temperature profile along a vertical plane crossing the center of the cavity.

emphasize that all elements of the method, from the derivation of equations and boundary conditions, to the reconditioning of the equations and the numerical method is accessible to higher moment numbers.

As an indicator for this, we have added our own calculations for the R20 equations into Fig. 3. We implemented the R20 equations as given in [40] together with the proper boundary conditions into our numerical scheme. As can be seen, the addition of more moments leads to a better description of the velocity profile close to the wall – we attribute this to the

additional Knudsen layer contribution in the sense of [49] that is present in the R20 equations. Detailed examinations of higher order moment equations is outside the scope of this paper.

Interestingly, for the 2D Navier–Stokes–Fourier case, when we use second order jump and slip conditions, the discrepancy to the exact solution is larger than for first order boundary conditions. This stands in contrast to the simulation of Poiseuille flows where the second order velocity slip boundary conditions yield marked improvement over the first order conditions, in particular the prediction of the Knudsen minimum, and the overall flow rate [33]. This behavior of NSF with 2nd order boundary conditions is consistent with the findings of [50,37], where it is shown that these boundary conditions are not necessarily useful in more general situations.

### 5.3. Global flow properties

Most often, one will not be interested in the very details of a process, but in some meaningful *global* flow properties. For the driven cavity, these are the mean dimensionless shear stress on the moving wall, $D$, and the dimensionless flow rate of the main vortex, $G$, defined as [6]

$$D = \int_0^1 \frac{\sigma_{ij}}{p_0}(x,1)dx, \quad \text{and} \quad G = \int_0^1 \frac{|v_x(1/2,y)|}{v_{lid}}dy. \tag{30}$$

Results of R13 and NSF models together with the IMM data of Sharipov et al. [6] are presented in Tables 1 and 2 for $D$ and $G$, respectively, with different values of the rarefaction parameter $\delta = \sqrt{\frac{1}{2}\frac{1}{\mathrm{Kn}}}$.

We could not find DSMC and IMM results for Knudsen numbers below 0.07, at rather small Knudsen number $Kn = 0.01$, R13 and NSF already show a relative difference of 7%. While lack of an exact solution does not permit us to judge whether R13 or NSF is more accurate at this small Knudsen number, the results for higher Knudsen numbers indicate the advantage is for R13: As the Knudsen number grows, NSF and R13 results differ more and more, where R13 agrees well with the exact solution (IMM) for Knudsen numbers up to 0.5, while NSF already has an error of more than 19% at $Kn = 0.07$. This behavior is a reflection of the order of the respective equations. NSF with slip and jump boundary conditions is of first order in the Knudsen number, and cannot be expected to give reliable results above $Kn = 0.05$. R13, on the other hand is of third order in $Kn$, and should give meaningful results up to $Kn \simeq \sqrt[3]{0.05} = 0.38$. For $Kn = 0.707$, R13 gives an error of less then 10%, while NSF with first and second order boundary conditions give an error of almost 50% and 60%, respectively. Clearly, both theories are outside their range of validity, but R13 still gives a reasonable estimate that should have value as an engineering approximation.

### 5.4. Field plots

Finally, Figs. 5 and 6 shows flow details for $Kn = 0.08$. Results computed with DSMC [42], R13, and NSF with first and second order boundary conditions are compared. Fig. 5 shows velocity streamlines superimposed on viscous shear stress contours. While the differences between the simulations are not marked, one can nevertheless see differences in the details. DSMC (Fig. 5(a)) and R13 (Fig. 5(b)) show relatively similar stress contours, which differ from the NSF contours (Fig. 5(c, d)). In particular, DSMC and R13 show more uniform stress fields at the upper and lower walls, whereas the NSF solutions show more variation along these walls.

The most notable difference between DSMC Fig. 6(a) and NSF Fig. 6(c, d), is the reverse direction of the heat flux. In the NSF results, Fourier's law forces the heat flux to point from hot to cold, along the negative temperature gradient. In the DSMC results, the direction is inverted, that is heat is transferred from cold to warm. In a DSMC solution, as in any numerical solution of the Boltzmann equation, this is an outcome of the simulation which cannot be further analyzed to increase understanding of the interaction of flow properties. This is different for the R13 equations, which show the same behavior as the DSMC results, i.e., a heat flux vector pointing from cold to warm.

### 5.5. Anti-Fourier heat flux

That this behavior appears from the moment system shows that it is a result of the collective behavior of particles, as expressed in the few moments (weighted averages of the velocity distribution function) considered. The heat flux is given by Eq. (3), and the question is which of the many terms lead to the inverted heat flow. We proceed with a discussion of the equation in terms of the process at hand, in order to isolate the most important terms. The first reduction comes from the observation that the driving force (the velocity of the lid) is relatively small, which implies that non-linear effects should

**Table 1**
Dimensionless shear stress, D on the moving wall vs Knudsen number for R13, NSF with 1st order BCs (NSF1) and 2nd order BCs (NSF2).

| Kn | $\delta$ | $D$ [6] | $D$ (R13) | $D$ (NSF1) | $D$ (NSF2) |
|---|---|---|---|---|---|
| 0.010 | 70.7 | – | 0.1585 | 0.1476 | 0.1416 |
| 0.071 | 10 | 0.415 – −0.417 | 0.4271 | 0.4967 | 0.4000 |
| 0.141 | 5 | 0.502 – −0.507 | 0.5084 | 0.6613 | 0.4474 |
| 0.354 | 2 | 0.580 – −0.592 | 0.5644 | 0.8554 | 0.3717 |
| 0.707 | 1 | 0.620 – −0.631 | 0.5722 | 0.9619 | 0.2533 |

**Table 2**
Dimensionless flow rate, G vs Knudsen number for R13, NSF with 1st order BCs (NSF1) and 2nd order BCs (NSF2).

| Kn | $\delta$ | $G$ [6] | $G$ (R13) | $G$ (NSF1) | $G$ (NSF2) |
|---|---|---|---|---|---|
| 0.010 | 70.7 | – | 0.1893 | 0.1878 | 0.1878 |
| 0.071 | 10 | 0.143–0.145 | 0.1428 | 0.1389 | 0.1298 |
| 0.141 | 5 | 0.127–0.128 | 0.1216 | 0.1077 | 0.0860 |
| 0.354 | 2 | 0.111–0.112 | 0.1044 | 0.0653 | 0.0323 |
| 0.707 | 1 | 0.104–0.106 | 0.1003 | 0.0397 | 0.0113 |

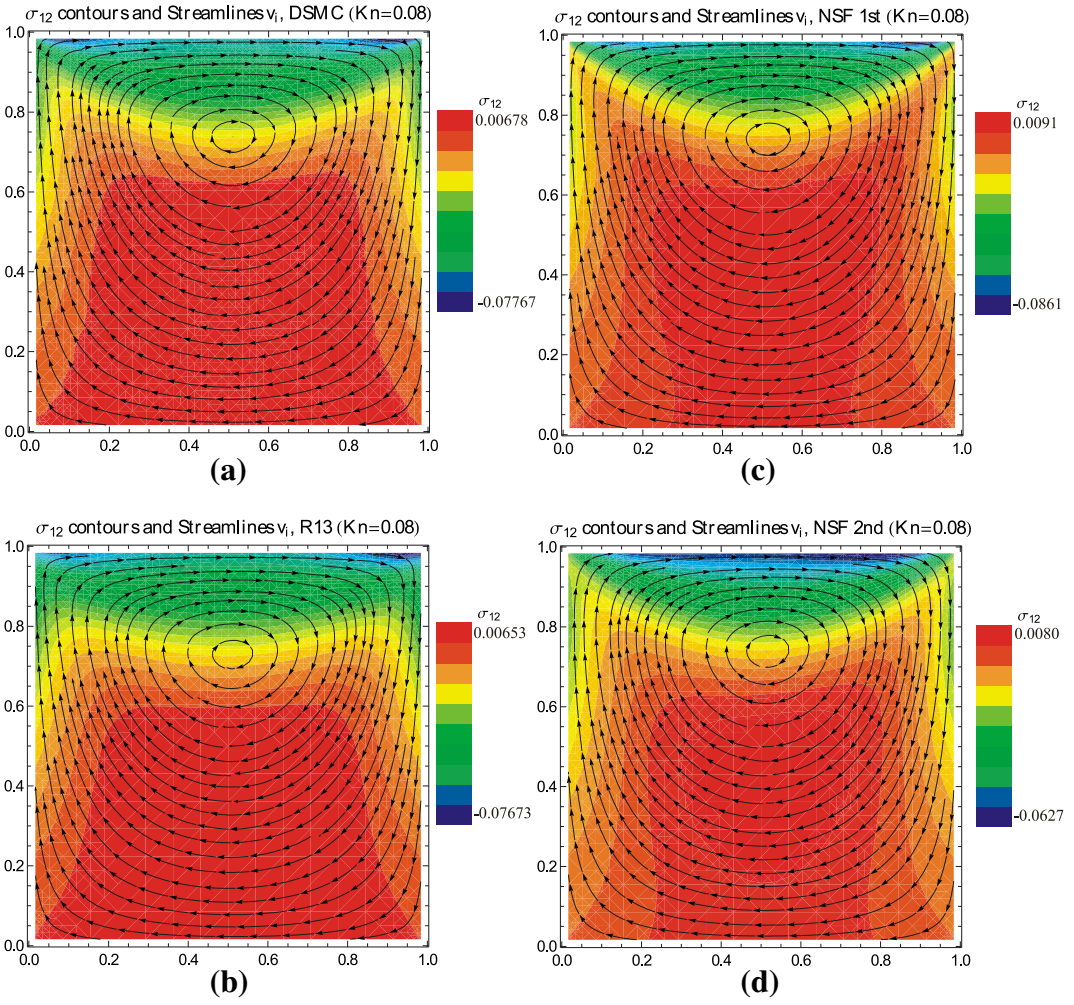


**Fig. 5.** *Streamlines superimposed on viscous shear stress $\sigma_{xy}$ contours with$Kn = 0.08$, $v_{lid} = 50\ m/s$.*

only play a minor role, and linear terms dominate. That is it suffices to look at the linearization of (3 ), which after use of (5) assumes the form

$$\theta\frac{\partial\sigma_{ik}}{\partial x_k}+\frac{5}{2}p\frac{\partial\theta}{\partial x_i}=-\frac{2}{3}\frac{p}{\mu}q_i+\frac{12}{5}\frac{\mu}{p}\theta\left[\frac{\partial^2 q_i}{\partial x_k\partial x_k}+\frac{\partial^2 q_k}{\partial x_i\partial x_k}\right]. \tag{31}$$

As can be seen from the detailed discussion in, e.g., Refs. [24,28,4,33,29], the derivative terms on the right hand side produce Knudsen layers. The results shown are for a relatively small Knudsen number $Kn = 0.08$, where the Knudsen layers are restricted to the regions close to the walls. Hence, for the explanation of the inverted heat flux, these terms are not relevant, and the heat flux in the bulk can be written as

$$q_i=-\frac{15}{4}\mu\frac{\partial\theta}{\partial x_i}-\frac{3}{2}\frac{\mu}{p}\theta\frac{\partial\sigma_{ik}}{\partial x_k}. \tag{32}$$

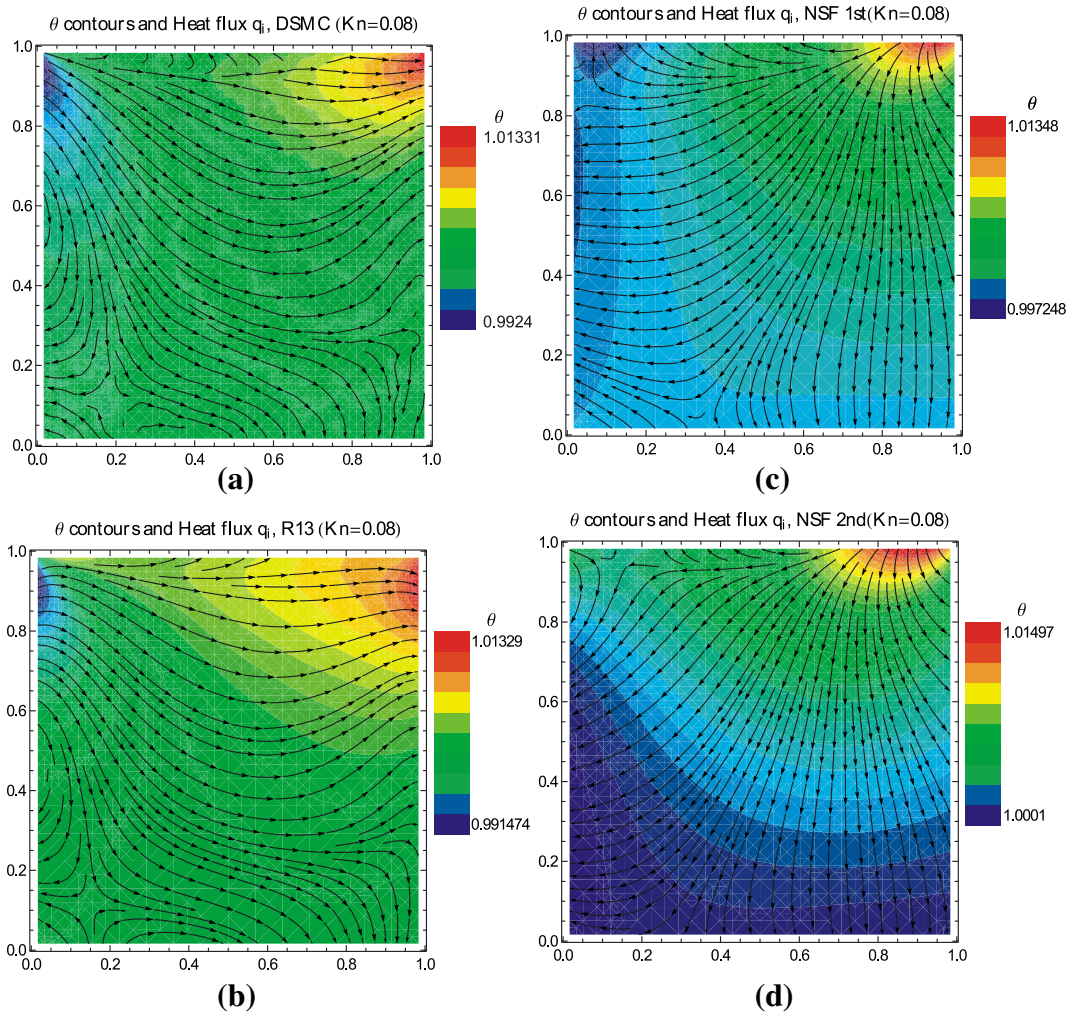


**Fig. 6.** *Heat flux superimposed on temperature* $\theta$ *contours with* $Kn = 0.08$, $v_{lid} = 50 m/s$.

Here, the first term is the well-known Fourier contribution to heat flux, which is of first order in the Knudsen number (first order in viscosity $\mu$ in dimensional form). The second term is a second order correction for the heat flux, which relates this to the gradient in stress. When one replaces the stress by means of the Navier–Stokes law (12), one finds terms with the second derivative of velocity which are well-known from the Burnett equations [20,4]. Close to the lid, the heat flux is mainly in $x$-direction, therefore we can have a look at $q_x$, which can be further written as

$$q_x = -\frac{15}{4}\mu\frac{\partial\theta}{\partial x} - \frac{3}{2}\frac{\mu}{p}\theta\frac{\partial\sigma_{xx}}{\partial x} - \frac{3}{2}\frac{\mu}{p}\theta\frac{\partial\sigma_{xy}}{\partial y}. \tag{33}$$

In the dimensionless quantities plotted in Figs. 5 and 6, this equation reads, after linearization,

$$q_x = -\frac{15}{4}\mathrm{Kn}\left[\frac{\partial\theta}{\partial x} + \frac{2}{5}\frac{\partial\sigma_{xx}}{\partial x} + \frac{2}{5}\frac{\partial\sigma_{xy}}{\partial y}\right]. \tag{34}$$

Our results indicate that the term $\frac{\partial\sigma_{xx}}{\partial x}$ is significantly smaller than the other two terms. Thus, the sign of $q_x$ depends on the relative size of $\frac{\partial\theta}{\partial x}$ and $\frac{2}{5}\frac{\partial\sigma_{xy}}{\partial y}$. Estimates for these gradients can be read directly from the figures: Looking at the top of Fig. 6(a) we estimate $\frac{\partial\theta}{\partial x} \simeq 0.021$, and looking at the centerline of Fig. 5(a), we estimate $\frac{\partial\sigma_{xy}}{\partial y} \simeq -0.084$, and hence $\frac{2}{5}\frac{\partial\sigma_{xy}}{\partial y} \simeq -0.034$. Thus, for these flow conditions, the stress gradient dominates, and as a result the heat flux points from cold to warm.

### 5.6. Comparison to other moment results

The lid-driven cavity problem was first calculated with the regularized 13-moment system as well as the enlarged regularized 20-moment system by Mizzi in [40] using boundary conditions from [38]. However, the simulation suffered from

oversubscribed boundary conditions, which led to oscillations for the field quantities at the wall. The problem of the right number of boundary conditions has been resolved in [28] and also the discussion in present paper.

In [41] the regularized 26-moment equations have been derived as an even more enlarged moment system which is expected to increase the accuracy further. The driven cavity problem was studied with the R26 equations in [42,43]. The boundary model for the walls follow the principles of [28], however, the actually numerical implementation is not explained in detail. In the results the Knudsen layer behavior for velocity is clearly superior to the R13 results presented above. As described in Section 5.2 the Knudsen layer of R13 consists of only one mode and the additional modes introduced by R20 or R26 increases the accuracy at the expense of more complex equations.

However, the heat flux pattern shown in [43] deviates clearly from the DSMC data and shows much less accuracy than the results of R13, even for small Knudsen number, like $Kn = 0.1$. The reason for this deviation remains unclear. Consequently, it is too early to conclude which moment model gives ultimately better results. Examination of extended moment systems are planned for the future.

## 6. Conclusion

We considered a specific example of a driven cavity flow using R13 equations and compared it with other theories such as NSF, DSMC and Integro-Moment methods. Following a detailed comparison with the integro-moment [6] and DSMC [42] methods, it is demonstrated that the R13 equations can be considered as a reliable alternative mathematical model to reduce the computational cost for complex industrial problems with small Mach number and moderate Knudsen number. In conclusion we point out that the R13 equations are an approximation to the Boltzmann equation, so that we cannot expect perfect agreement. Nevertheless, the equations exhibit good agreement, which includes the reproduction of all flow features, including all rarefaction effects, like Knudsen layers and anti-Fourier heat flux, and small relative errors.

In the present paper we also derived a theory of boundary conditions for the regularized 13-moment equations by using the order of magnitude argument to rewrite the non-linear part of the equations such that the linear and non-linear equations require the same boundary conditions.

## Appendix A. Matrix structure

The original R13 equations (1)–(4 and (5) can be written in the matrix form as

$$\mathcal{A}(U)\frac{\partial U}{\partial x}+\mathcal{B}(U)\frac{\partial U}{\partial y}+\frac{1}{Kn}P(U)U=0.$$

Here, matrices $\mathcal{A}(U)$ and $P(U)$are given by

$$\mathcal{A}(U)=\begin{pmatrix}
v_1 & \rho & 0 & 0 & 0 & 0 & 0 & 0 & 0 & 0 & 0 & 0 & 0 & 0 & 0 & 0\\
\theta & \rho v_1 & 0 & \rho & 0 & 0 & 1 & 0 & 0 & 0 & 0 & 0 & 0 & 0 & 0 & 0\\
0 & 0 & \rho v_1 & 0 & 0 & 0 & 0 & 1 & 0 & 0 & 0 & 0 & 0 & 0 & 0 & 0\\
0 & \theta\rho+\sigma_{11} & \sigma_{12} & \frac{3\rho v_1}{2} & 1 & 0 & 0 & 0 & 0 & 0 & 0 & 0 & 0 & 0 & 0 & 0\\
-\frac{\theta\sigma_{11}}{\rho} & m_{111}+\frac{16q_1}{5} & m_{112}+\frac{2q_2}{5} & \frac{5\theta\rho}{2}+\frac{5\sigma_{11}}{2} & v_1 & 0 & \theta-\frac{\sigma_{11}}{\rho} & -\frac{\sigma_{12}}{\rho} & 0 & \frac{1}{2} & 0 & 0 & 0 & 0 & 0 & \frac{1}{6}\\
-\frac{\theta\sigma_{12}}{\rho} & m_{112}+\frac{7q_2}{5} & m_{122}+\frac{7q_1}{5} & \frac{5\sigma_{12}}{2} & 0 & v_1 & -\frac{\sigma_{12}}{\rho} & \theta-\frac{\sigma_{22}}{\rho} & 0 & 0 & \frac{1}{2} & 0 & 0 & 0 & 0 & 0\\
0 & \frac{4\theta\rho}{3}+\frac{7\sigma_{11}}{3} & -\frac{2\sigma_{12}}{3} & 0 & \frac{8}{15} & 0 & v_1 & 0 & 0 & 0 & 0 & 0 & 1 & 0 & 0 & 0\\
0 & 2\sigma_{12} & \theta\rho+\sigma_{11} & 0 & 0 & \frac{2}{5} & 0 & v_1 & 0 & 0 & 0 & 0 & 0 & 1 & 0 & 0\\
0 & -\frac{2\theta\rho}{3}-\frac{2\sigma_{11}}{3}+\sigma_{22} & \frac{4\sigma_{12}}{3} & 0 & -\frac{4}{15} & 0 & 0 & 0 & v_1 & 0 & 0 & 0 & 0 & 0 & 1 & 0\\
-\frac{2\theta q_1}{3\rho} & \frac{10\theta\sigma_{11}}{21} & \frac{5\theta\sigma_{12}}{21} & \frac{2q_1}{3} & \frac{2\theta}{3} & 0 & 0 & 0 & 0 & 0 & 0 & 0 & 0 & 0 & 0 & 0\\
-\frac{\theta q_2}{2\rho} & \frac{5\theta\sigma_{12}}{21} & \frac{5}{14}\theta(\sigma_{11}+\sigma_{22}) & \frac{q_2}{2} & 0 & \frac{\theta}{2} & 0 & 0 & 0 & 0 & 0 & 0 & 0 & 0 & 0 & 0\\
\frac{\theta q_1}{3\rho} & -\frac{10}{21}\theta(\sigma_{11}+\sigma_{22}) & \frac{5\theta\sigma_{12}}{21} & -\frac{q_1}{3} & -\frac{\theta}{3} & 0 & 0 & 0 & 0 & 0 & 0 & 0 & 0 & 0 & 0 & 0\\
-\frac{3\theta\sigma_{11}}{5\rho} & \frac{8q_1}{25} & -\frac{4q_2}{25} & 0 & 0 & 0 & \frac{3\theta}{5} & 0 & 0 & 0 & 0 & 0 & 0 & 0 & 0 & 0\\
-\frac{8\theta\sigma_{12}}{15\rho} & \frac{16q_2}{75} & \frac{16q_1}{75} & 0 & 0 & 0 & 0 & \frac{8\theta}{15} & 0 & 0 & 0 & 0 & 0 & 0 & 0 & 0\\
-\frac{\theta(5\sigma_{22}-2\sigma_{11})}{15\rho} & -\frac{4q_1}{25} & \frac{16q_2}{75} & 0 & 0 & 0 & -\frac{2\theta}{15} & 0 & \frac{\theta}{3} & 0 & 0 & 0 & 0 & 0 & 0 & 0\\
\frac{2\theta\sigma_{12}}{5\rho} & -\frac{4q_2}{25} & -\frac{4q_1}{25} & 0 & 0 & 0 & 0 & -\frac{2\theta}{5} & 0 & 0 & 0 & 0 & 0 & 0 & 0 & 0\\
-\frac{8\theta q_1}{\rho} & 8\theta\sigma_{11} & 8\theta\sigma_{12} & 20q_1 & 8\theta & 0 & 0 & 0 & 0 & 0 & 0 & 0 & 0 & 0 & 0 & 0
\end{pmatrix}$$

and

$$\mathcal{P}(U) = \begin{pmatrix}
0 & 0 & 0 & 0 & 0 & 0 & 0 & 0 & 0 & 0 & 0 & 0 & 0 & 0 & 0 & 0 \\
0 & 0 & 0 & 0 & 0 & 0 & 0 & 0 & 0 & 0 & 0 & 0 & 0 & 0 & 0 & 0 \\
0 & 0 & 0 & 0 & 0 & 0 & 0 & 0 & 0 & 0 & 0 & 0 & 0 & 0 & 0 & 0 \\
0 & 0 & 0 & 0 & 0 & 0 & 0 & 0 & 0 & 0 & 0 & 0 & 0 & 0 & 0 & 0 \\
0 & 0 & 0 & 0 & \frac{2}{3} & 0 & 0 & 0 & 0 & 0 & 0 & 0 & 0 & 0 & 0 & 0 \\
0 & 0 & 0 & 0 & 0 & \frac{2}{3} & 0 & 0 & 0 & 0 & 0 & 0 & 0 & 0 & 0 & 0 \\
0 & 0 & 0 & 0 & 0 & 0 & 1 & 0 & 0 & 0 & 0 & 0 & 0 & 0 & 0 & 0 \\
0 & 0 & 0 & 0 & 0 & 0 & 0 & 1 & 0 & 0 & 0 & 0 & 0 & 0 & 0 & 0 \\
0 & 0 & 0 & 0 & 0 & 0 & 0 & 0 & 1 & 0 & 0 & 0 & 0 & 0 & 0 & 0 \\
0 & 0 & 0 & 0 & 0 & 0 & \frac{5(\sigma_{11}-\sigma_{22})}{126\rho} & \frac{5\sigma_{12}}{126\rho} & -\frac{5(\sigma_{11}+2\sigma_{22})}{126\rho} & \frac{5}{24} & 0 & 0 & 0 & 0 & 0 & 0 \\
0 & 0 & 0 & 0 & 0 & 0 & \frac{5\sigma_{12}}{84\rho} & \frac{5(\sigma_{11}+\sigma_{22})}{84\rho} & \frac{5\sigma_{12}}{84\rho} & 0 & \frac{5}{24} & 0 & 0 & 0 & 0 & 0 \\
0 & 0 & 0 & 0 & 0 & 0 & -\frac{5(2\sigma_{11}+\sigma_{22})}{126\rho} & \frac{5\sigma_{12}}{126\rho} & -\frac{5(\sigma_{11}-\sigma_{22})}{126\rho} & 0 & 0 & \frac{5}{24} & 0 & 0 & 0 & 0 \\
0 & 0 & 0 & 0 & 0 & 0 & 0 & 0 & 0 & 0 & 0 & 0 & \frac{1}{2} & 0 & 0 & 0 \\
0 & 0 & 0 & 0 & 0 & 0 & 0 & 0 & 0 & 0 & 0 & 0 & 0 & \frac{1}{2} & 0 & 0 \\
0 & 0 & 0 & 0 & 0 & 0 & 0 & 0 & 0 & 0 & 0 & 0 & 0 & 0 & \frac{1}{2} & 0 \\
0 & 0 & 0 & 0 & 0 & 0 & 0 & 0 & 0 & 0 & 0 & 0 & 0 & 0 & 0 & \frac{1}{2} \\
0 & 0 & 0 & 0 & 0 & 0 & \frac{2(2\sigma_{11}+\sigma_{22})}{3\rho} & \frac{4\sigma_{12}}{3\rho} & \frac{2(\sigma_{11}+2\sigma_{22})}{3\rho} & 0 & 0 & 0 & 0 & 0 & 0 & \frac{2}{3}
\end{pmatrix}$$

The matrix $\mathcal{B}(U)$can be constructed analogous to $\mathcal{A}(U)$, therefore, we will not show it here. The transformed system results after eliminating the Navier–Stokes stress and the Fourier heat flux by the actual stress and heat flux, as described in Section 4.1, reduced matrices $\mathcal{A}(U)$ and $P(U)$ read.

$$\mathcal{A}(U) = \begin{pmatrix}
v_1 & \rho & 0 & 0 & 0 & 0 & 0 & 0 & 0 & 0 & 0 & 0 & 0 & 0 & 0 & 0 \\
\theta & \rho v_1 & 0 & \rho & 0 & 0 & 1 & 0 & 0 & 0 & 0 & 0 & 0 & 0 & 0 & 0 \\
0 & 0 & \rho v_1 & 0 & 0 & 0 & 0 & 1 & 0 & 0 & 0 & 0 & 0 & 0 & 0 & 0 \\
0 & \theta\rho + \sigma_{11} & \sigma_{12} & \frac{3\rho v_1}{2} & 1 & 0 & 0 & 0 & 0 & 0 & 0 & 0 & 0 & 0 & 0 & 0 \\
-\frac{\theta\sigma_{11}}{\rho} & m_{111} + \frac{16 q_1}{5} & m_{112} + \frac{2 q_2}{5} & \frac{5\theta\rho}{2} + \frac{5\sigma_{11}}{2} & v_1 & 0 & \theta - \frac{\sigma_{11}}{\rho} & -\frac{\sigma_{12}}{\rho} & 0 & \frac{1}{2} & 0 & 0 & 0 & 0 & 0 & \frac{1}{6} \\
-\frac{\theta\sigma_{12}}{\rho} & m_{112} + \frac{7 q_2}{5} & m_{122} + \frac{7 q_1}{5} & \frac{5\sigma_{12}}{2} & 0 & v_1 & -\frac{\sigma_{12}}{\rho} & \theta - \frac{\sigma_{22}}{\rho} & 0 & 0 & \frac{1}{2} & 0 & 0 & 0 & 0 & 0 \\
0 & \frac{4\theta\rho}{3} + \frac{7\sigma_{11}}{3} & -\frac{2\sigma_{12}}{3} & 0 & \frac{8}{15} & 0 & v_1 & 0 & 0 & 0 & 0 & 0 & 1 & 0 & 0 & 0 \\
0 & 2\sigma_{12} & \theta\rho + \sigma_{11} & 0 & 0 & \frac{2}{5} & 0 & v_1 & 0 & 0 & 0 & 0 & 0 & 1 & 0 & 0 \\
0 & -\frac{2\theta\rho}{3} - \frac{2\sigma_{11}}{3} + \sigma_{22} & \frac{4\sigma_{12}}{3} & 0 & -\frac{4}{15} & 0 & 0 & 0 & v_1 & 0 & 0 & 0 & 0 & 0 & 1 & 0 \\
-\frac{2\theta q_1}{3\rho} & 0 & 0 & -\frac{2 q_1}{3} & \frac{2\theta}{3} & 0 & 0 & 0 & 0 & 0 & 0 & 0 & 0 & 0 & 0 & 0 \\
-\frac{\theta q_2}{2\rho} & 0 & 0 & -\frac{q_2}{2} & 0 & \frac{\theta}{2} & 0 & 0 & 0 & 0 & 0 & 0 & 0 & 0 & 0 & 0 \\
\frac{\theta q_1}{3\rho} & 0 & 0 & \frac{q_1}{3} & -\frac{\theta}{3} & 0 & 0 & 0 & 0 & 0 & 0 & 0 & 0 & 0 & 0 & 0 \\
-\frac{3\theta\sigma_{11}}{5\rho} & 0 & 0 & -\frac{3\sigma_{11}}{5} & 0 & 0 & \frac{3\theta}{5} & 0 & 0 & 0 & 0 & 0 & 0 & 0 & 0 & 0 \\
-\frac{8\theta\sigma_{12}}{15\rho} & 0 & 0 & -\frac{8\sigma_{12}}{15} & 0 & 0 & 0 & \frac{8\theta}{15} & 0 & 0 & 0 & 0 & 0 & 0 & 0 & 0 \\
-\frac{\theta(5\sigma_{22}-2\sigma_{11})}{15\rho} & 0 & 0 & \frac{1}{15}(2\sigma_{11} - 5\sigma_{22}) & 0 & 0 & -\frac{2\theta}{15} & 0 & \frac{\theta}{3} & 0 & 0 & 0 & 0 & 0 & 0 & 0 \\
\frac{2\theta\sigma_{12}}{5\rho} & 0 & 0 & \frac{2\sigma_{12}}{5} & 0 & 0 & 0 & -\frac{2\theta}{5} & 0 & 0 & 0 & 0 & 0 & 0 & 0 & 0 \\
-\frac{8\theta q_1}{\rho} & 0 & 0 & -8 q_1 & 8\theta & 0 & 0 & 0 & 0 & 0 & 0 & 0 & 0 & 0 & 0 & 0
\end{pmatrix}$$

and

$$\mathcal{P}(U) = \begin{pmatrix}
0&0&0&0&0&0&0&0&0&0&0&0&0&0&0&0&0&0\\
0&0&0&0&0&0&0&0&0&0&0&0&0&0&0&0&0&0\\
0&0&0&0&0&0&0&0&0&0&0&0&0&0&0&0&0&0\\
0&0&0&0&0&0&0&0&0&0&0&0&0&0&0&0&0&0\\
0&0&0&0&\frac{2}{3}&0&0&0&0&0&0&0&0&0&0&0&0&0\\
0&0&0&0&0&\frac{2}{3}&0&0&0&0&0&0&0&0&0&0&0&0\\
0&0&0&0&0&0&1&0&0&0&0&0&0&0&0&0&0&0\\
0&0&0&0&0&0&0&1&0&0&0&0&0&0&0&0&0&0\\
0&0&0&0&0&0&0&0&1&0&0&0&0&0&0&0&0&0\\
0&0&0&0&-\frac{16q_1}{45\theta\rho}&\frac{8q_2}{45\theta\rho}&-\frac{25(\sigma_{11}-\sigma_{22})}{126\rho}&-\frac{25\sigma_{12}}{126\rho}&\frac{25(\sigma_{11}+2\sigma_{22})}{126\rho}&\frac{5}{24}&0&0&0&0&0&0&0&0\\
0&0&0&0&-\frac{4q_2}{15\theta\rho}&-\frac{4q_1}{15\theta\rho}&-\frac{25\sigma_{12}}{84\rho}&-\frac{25(\sigma_{11}+\sigma_{22})}{84\rho}&-\frac{25\sigma_{12}}{84\rho}&0&\frac{5}{24}&0&0&0&0&0&0&0\\
0&0&0&0&\frac{8q_1}{45\theta\rho}&-\frac{16q_2}{45\theta\rho}&\frac{25(2\sigma_{11}+\sigma_{22})}{126\rho}&-\frac{25\sigma_{12}}{126\rho}&\frac{25(\sigma_{11}-\sigma_{22})}{126\rho}&0&0&\frac{5}{24}&0&0&0&0&0&0\\
0&0&0&0&-\frac{6\sigma_{11}}{25\theta\rho}&\frac{4\sigma_{12}}{25\theta\rho}&-\frac{4q_1}{25\theta\rho}&\frac{8q_2}{75\theta\rho}&0&0&0&0&\frac{1}{2}&0&0&0&0&0\\
0&0&0&0&-\frac{16\sigma_{12}}{75\theta\rho}&-\frac{2(5\sigma_{11}-2\sigma_{22})}{75\theta\rho}&-\frac{4q_2}{45\theta\rho}&-\frac{32q_1}{225\theta\rho}&\frac{8q_2}{225\theta\rho}&0&0&0&0&\frac{1}{2}&0&0&0&0\\
0&0&0&0&\frac{2(2\sigma_{11}-5\sigma_{22})}{75\theta\rho}&-\frac{16\sigma_{12}}{75\theta\rho}&\frac{8q_1}{225\theta\rho}&-\frac{32q_2}{225\theta\rho}&-\frac{4q_1}{45\theta\rho}&0&0&0&0&0&\frac{1}{2}&0&0&0\\
0&0&0&0&\frac{4\sigma_{12}}{25\theta\rho}&-\frac{6\sigma_{22}}{25\theta\rho}&0&\frac{8q_1}{75\theta\rho}&-\frac{4q_2}{25\theta\rho}&0&0&0&0&0&0&\frac{1}{2}&0\\
0&0&0&0&-\frac{112q_1}{15\theta\rho}&-\frac{112q_2}{15\theta\rho}&-\frac{10(2\sigma_{11}+\sigma_{22})}{3\rho}&-\frac{20\sigma_{12}}{3\rho}&-\frac{10(\sigma_{11}+2\sigma_{22})}{3\rho}&0&0&0&0&0&0&0&\frac{2}{3}
\end{pmatrix}$$

respectively. Also the boundary conditions, for the wall normal pointing toward $x$-direction, are being recasted into

$$U = \mathcal{X}(U)U + \mathcal{X}^d,$$

with matrices

$$\mathcal{X}(U) = \begin{pmatrix}
1&0&0&0&0&0&0&0&0&0&0&0&0&0&0&0&0&0\\
0&0&0&0&0&0&0&0&0&0&0&0&0&0&0&0&0&0\\
0&0&1&0&0&0&0&0&0&0&0&0&0&0&0&0&0&0\\
0&0&0&1&0&0&0&0&0&0&0&0&0&0&0&0&0&0\\
0&0&0&-2\xi\mathcal{P}n_x&0&0&-\frac{1}{2}\theta\xi n_x&0&0&-\frac{5\xi n_z}{28}&0&0&0&0&0&0&-\frac{\xi n_z}{15}\\
0&0&0&0&0&1&0&0&0&0&0&0&0&0&0&0&0&0\\
0&0&0&0&0&0&1&0&0&0&0&0&0&0&0&0&0&0\\
0&0&\xi(-\mathcal{P})n_x&0&0&-\frac{\xi n_z}{5}&0&0&0&0&0&0&0&-\frac{\xi n_z}{2}&0&0&0\\
0&0&0&0&0&0&0&0&1&0&0&0&0&0&0&0&0&0\\
0&0&0&0&0&0&0&0&0&1&0&0&0&0&0&0&0&0\\
0&0&7\theta\xi\mathcal{P}n_x&0&0&-\frac{11}{5}\theta\xi n_x&0&0&0&0&0&0&0&-\frac{1}{2}\theta\xi n_x&0&0&0\\
0&0&0&0&0&0&0&0&0&0&0&1&0&0&0&0&0&0\\
0&0&0&\frac{2\xi\mathcal{P}n_z}{5}&0&0&-\frac{7}{5}\theta\xi n_x&0&0&-\frac{\xi n_z}{14}&0&0&0&0&0&0&\frac{\xi n_z}{75}\\
0&0&0&0&0&0&0&0&0&0&0&0&1&0&0&0&0&0\\
0&0&0&-\frac{1}{5}\xi\mathcal{P}n_x&0&0&\frac{\theta\xi n_z}{5}&0&-\theta\xi n_x&0&0&-\frac{\xi n_z}{14}&0&0&0&0&-\frac{\xi n_z}{150}\\
0&0&0&0&0&0&0&0&0&0&0&0&0&0&0&1&0&0\\
0&0&0&0&0&0&0&0&0&0&0&0&0&0&0&0&0&1
\end{pmatrix}$$

*and* $\mathcal{X}^d(U) = \begin{pmatrix}
0\\0\\0\\0\\\frac{1}{2}\xi\mathcal{P}n_x\left(\mathcal{V}_2{}^2+4\theta^W\right)\\0\\0\\\xi\mathcal{P}n_x v_2{}^W\\0\\0\\\xi(-\mathcal{P})n_x\left(6\mathcal{V}_2\theta^W+\mathcal{V}_2{}^3+7\theta v_2{}^W\right)\\0\\-\frac{1}{5}\xi\mathcal{P}n_x\left(3\mathcal{V}_2{}^2+2\theta^W\right)\\0\\\frac{1}{5}\xi\mathcal{P}n_x\left(4\mathcal{V}_2{}^2+\theta^W\right)\\0\\0
\end{pmatrix}$

where, $\xi = \frac{\chi}{2-\chi}\sqrt{\frac{2}{\pi\theta}}$.

## Appendix B. Second order boundary conditions for NSF

We find a second-order jump and slip boundary conditions for NSF by combining the Eqs. (7a)–(7c) and (13) and replacing the stress tensor and heat flux vector using second order contributions given by the Burnett equations [4]. Note that Burnett equations can be obtained from 13 moment equations by CE expansion [4]. Considering the leading linear terms only, we obtain

$$v_n = 0, \tag{35a}$$

$$\sigma_{\tau n}^{NSF} = \frac{-\chi}{2-\chi}\sqrt{\frac{2}{\pi\theta}}\left(\mathcal{P}\mathcal{V}_\tau + \frac{1}{5}q_\tau^{NSF} + \frac{m_{\tau nn}^{(2)}}{2} + \frac{1}{5}\frac{\mu^2}{\rho}\left(\frac{45}{16}\frac{\partial^2 v_\tau}{\partial x_k \partial x_k} - \frac{13}{4}\frac{\partial^2 v_k}{\partial x_k \partial x_\tau}\right)\right) - \frac{1}{18}\frac{R_{\tau n}^{(2)}}{\theta}, \tag{35b}$$

$$q_n^{NSF} = \frac{-\chi}{2-\chi}\sqrt{\frac{2}{\pi\theta}}\left(2\mathcal{P}\mathcal{T} - \frac{1}{2}\mathcal{P}\mathcal{V}_\tau^2 + \frac{1}{2}\theta\sigma_{nn}^{NSF} + \frac{1}{15}\Delta^{(2)} + \frac{13}{63}R_{nn}^{(2)}\right) - \frac{\mu^2}{\rho}\left(\frac{45}{16}\frac{\partial^2 v_n}{\partial x_k \partial x_k} - \frac{13}{4}\frac{\partial^2 v_k}{\partial x_k \partial x_n}\right), \tag{35c}$$

where the second order corrections, $m_{ijk}^{(2)}, \Delta^{(2)}$ and $R_{ij}^{(2)}$ result from the linear contributions of R13 constitutive relations (5) by replacing stress $\sigma_{ij}$ and heat flux $q_i$ with their Navier–Stokes–Fourier expressions,

$$\Delta^{(2)} = -12\frac{\mu}{\rho}\frac{\partial q_k^{NSF}}{\partial x_k}, R_{ij}^{(2)} = -\frac{24}{5}\frac{\mu}{\rho}\frac{\partial q_{\langle i}^{NSF}}{\partial x_{j\rangle}}, \quad \text{and} \quad m_{ijk}^{(2)} = -2\frac{\mu}{\rho}\frac{\partial \sigma_{\langle ij}^{NSF}}{\partial x_{k\rangle}}. \tag{36}$$

It can be seen that the form of (35) is the same as that of Sone's BC for flat interfaces [3], only that the R13 equations yield different coefficients then those given by Sone. We point out that the reduction of R13 with BC to jump and slip conditions for NSF or Burnett is somewhat ad hoc. Note that the larger system (R13) mathematically requires more boundary conditions then an asymptotic smaller system (NSF or Burnett). In general, it is not straight forward to develop a unique way to reduce the boundary conditions for the extended system to the smaller system. A detailed analysis of this, which should include comparison to Sone's work, is outside the scope of the present article and will be considered somewhere else in the future.

## References


[1] M. Gad-el-Hak, The MEMS Handbook, vols. I–III, 2nd ed., CRC Press, Boca Raton, FL, 2005.
[2] G.E. Karniadakis, A. Beskok, Micro Flows: Fundamentals and Simulation, Springer, New York, 2002.
[3] Y. Sone, Kinetic Theory and Fluid Dynamics, Birkhäuser, Boston, 2002.
[4] H. Struchtrup, Macroscopic Transport Equations for Rarefied Gas Flows, Springer, New York, 2005.
[5] H. Struchtrup, P. Taheri, Macroscopic transport models for rarefied gas flows: a brief review, IMA J. Appl. Math. 76 (2011) 672–697.
[6] S. Varoutis, D. Valougeorgis, F. Sharipov, Application of the integro-moment method to steady-state two-dimensional rarefied gas flows subject to boundary induced discontinuities, J. Comput. Phys. 227 (2008) 6272–6287.
[7] F. Sharipov, V. Seleznev, Data on internal rarefied gas flows, J. Phys. Chem. Ref. Data 27 (1998) 657–706.
[8] T. Ohwada, Y. Sone, K. Aoki, Numerical analysis of the Poiseuille and thermal transpiration flows between two parallel plates on the basis of the Boltzmann equation for hard sphere molecules, Phys. Fluids A 1 (1989) 2042–2049.
[9] S.K. Loyalka, Temperature jump and thermal creep slip: rigid sphere gas, Phys. Fluids A 1 (1989) 403–408.
[10] V.V. Aristov, Methods of Direct Solving the Boltzmann Equation and Study of Nonequilibrium Flows, Kluwer Academic Publishers, (US), 2001.
[11] V.A. Titarev, Conservative numerical methods for model kinetic equations, Comput. Fluids 36 (2007) 1446–1459.
[12] G.A. Bird, Molecular Gas Dynamics and the Direct Simulation of Gas Flows, Oxford University Press, Oxford, 1994.
[13] N.G. Hadjiconstantinou, A.L. Garcia, Statistical error in particle simulations of low Mach number flows, Proceedings of the First MIT Conference on Computational Fluid and Solid Mechanics, Elsevier, 2001.
[14] Jian-Zheng Jiang, J. Fan, Ching Shen, Statistical simulation of micro-cavity flows, in: Proc. of the 23rd International Symposium, RGD, 2003.
[15] T.M.M. Homolle, N.G. Hadjiconstantinou, Low-variance deviational simulation Monte Carlo, Phys. Fluids 19 (2007) 041701.
[16] T.M.M. Homolle, N.G. Hadjiconstantinou, A low-variance deviational simulation Monte Carlo for the Boltzmann equation, J. Comput. Phys. 226 (2007) 2341–2358.
[17] G.A. Radtke, N.G. Hadjiconstantinou, W. Wagner, Low-noise Monte Carlo simulation of the variable hard sphere gas, Phys. Fluids 23 (2011) 030606.
[18] S. Chapman, T.G. Cowling, The Mathematical Theory of Non-Uniform Gases, Cambridge University Press, Cambridge, 1970.
[19] H. Grad, On the kinetic theory of rarefied gases, Comm.Pure Appl.Math. 2 (1949) 331–407.
[20] D. Burnett, The distribution of molecular velocities and the mean motion in a non-uniform gas, Proc. Lond. Math. Soc. 40 (1936) 382–435.
[21] A.V. Bobylev, The Chapman–Enskog and Grad methods for solving the Boltzmann equation, Sov. Phys. Dokl. 27 (1982) 29–31.
[22] A.V. Bobylev, Instabilities in the Chapman–Enskog expansion and hyperbolic Burnett equations, J. Stat. Phys. 124 (2–4) (2006) 371–399.
[23] J.D. Au, M. Torrilhon, W. Weiss, The shock tube study in extended thermodynamics, Phys. Fluids 13 (2001) 2423–2432.
[24] H. Struchtrup, M. Torrilhon, Regularization of Grad's 13-moment-equations: derivation and linear analysis, Phys. Fluids 15 (2003) 668–2680.
[25] M. Torrilhon, H. Struchtrup, Regularized 13-moment-equations: shock structure calculations and comparison to Burnett models, J. Fluid Mech. 513 (2004) 171–198.
[26] M. Torrilhon, Two-dimensional bulk microflow simulations based on regularized 13-moment-equations, SIAM Multiscale Model. Simul. 5 (2006) 695–728.
[27] H. Struchtrup, M. Torrilhon, H-theorem, regularization, and boundary conditions for linearized 13 moment equations, Phys. Rev. Lett. 99 (2007) 014502.
[28] M. Torrilhon, H. Struchtrup, Boundary conditions for regularized 13-moment-equations for micro-channel-flows, J. Comp. Phys. 227 (2008) 1982–2011.
[29] P. Taheri, M. Torrilhon, H. Struchtrup, Couette and Poiseuille microflows: analytical solutions for regularized 13-moment equations, Phys. Fluids 21 (2009) 017102.
[30] P. Taheri, H. Struchtrup, Rarefaction effects in thermally-driven microflows, Physica A 389 (2010) 3069–3080.
[31] P. Taheri, A.S. Rana, M. Torrilhon, H. Struchtrup, Macroscopic description of steady and unsteady rarefaction effects in boundary value problems of gas dynamics, Continuum Mech. Thermodyn. 21 (2009) 423–443.
[32] H. Struchtrup, Resonance in rarefied gases, Cont. Mech. Thermodyn. published online (2012), http://dx.doi.org/10.1007/s00161-011-0202-0.
[33] H. Struchtrup, M. Torrilhon, Higher-order effects in rarefied channel flows, Phys. Rev. E 78 (2008) 046301.
[34] P. Taheri, H. Struchtrup, Effects of rarefaction in microflows between coaxial cylinders, Phys. Rev. E 80 (2009) 066317.
[35] P. Taheri, H. Struchtrup, An extended macroscopic transport model for rarefied gas flows in long capillaries with circular cross section, Phys. Fluids 22 (2010) 112004.
[36] P. Taheri, H. Struchtrup, Poiseuille flow of moderately rarefied gases in annular channels, Int. J. Heat Mass Transfer 55 (2012) 1291–1303.
[37] M. Torrilhon, Slow gas microflow past a sphere: analytical solution based on moment equations, Phys. Fluids 22 (2010) 072001.
[38] X. Gu, D. Emerson, A computational strategy for the regularized 13 moment equations with enhanced wall-boundary conditions, J. Comput. Phys. 225 (2007) 263–283.
[39] H. Struchtrup, Scaling and expansion of moment equations in kinetic theory, J. Stat. Phys. 125 (2006) 565–587.
[40] Simon Mizzi, Extended macroscopic models for rarefied gas dynamics in micro-sized domains, Ph.D. Thesis, University of Strathclyde, 2008.

[41] X.J. Gu, D.R. Emerson, A high-order moment approach for capturing non-equilibrium phenomena in the transition regime, J. Fluid Mech. 636 (2009) 177–216.
[42] B. John, X.J. Gu, D.R. Emerson, Investigation of heat and mass transfer in a lid-driven cavity under nonequilibrium flow conditions, Numer. Heat Transfer B: Fundam. 58 (2010) 287–303.
[43] X.J. Gu, B. John, G.H. Tang, D.R. Emerson, Heat and mass transfer of a rarefied gas in a driven micro.cavity, in: Proc. 2nd Micro/Nanoscale Heat and Mass Transfer International Conference, Shangha, MNHMT2009-18236i, 2009.
[44] K. Xu, Juan-Chen Huang, A unified gas-kinetic scheme for continuum and rarefied flows, J. Comput. Phys. 229 (2010) 7747–7764.
[45] J.C. Huang, K. Xu, P.B. Yu, A unified gas-kinetic scheme for continuum and rarefied flows. II: Multi-dimensional cases, Comm. Comput. Phys. 3 (2012) 662–690.
[46] M. Dehghan, Numerical procedures for a boundary value problem with a non-linear boundary condition, Appl. Math. Comput. 147 (2004) 291–306.
[47] M. Dehghan, Alternating direction implicit methods for two-dimensional diffusion with a nonlocal boundary condition, Int. J. Comput. Math. 72 (1999) 349–366.
[48] R. Freund, N. Nachtigal, QMR: A quasi-minimal residual method for non-Hermitian linear systems, Numer. Math. 60 (1991) 315–339.
[49] H. Struchtrup, Linear kinetic heat transfer: moment equations boundary conditions and Knudsen layers, Physica A 387 (2008) 1750–1766.
[50] A. Mohammadzadeh, E. Roohi, H. Niazmand, S.K. Stefanov, Detailed investigation of thermal and hydrodynamic flow behaviour in micro/nano cavity using DSMC and NSF equation, in: Proceedings of the ASME 2011 9th ICNMM2011, 2011.